Eur. Phys. J. A **28**, 63–82 (2006)
DOI 10.1140/epja/i2006-10011-3

THE EUROPEAN PHYSICAL JOURNAL A

On the strangeness −1 S-wave meson-baryon scattering

J.A. Oller[a]

Departamento de Física, Universidad de Murcia, E-30071 Murcia, Spain

Received: 17 March 2006 /
Published online: 10 May 2006 –
Communicated by U.-G. Meißner

Abstract. We consider meson-baryon interactions in S-wave with strangeness -1. This is a non-perturbative sector populated by plenty of resonances interacting in several two-body coupled channels. We study this sector combining a large set of experimental data. The recent experiments are remarkably accurate demanding a sound theoretical description to account for all the data. We employ unitary chiral perturbation theory up to and including $\mathcal{O}(p^2)$ to accomplish this aim. The spectroscopy of our solutions is studied within this approach, discussing the rise from the pole content of the two $\Lambda(1405)$ resonances and of the $\Lambda(1670)$, $\Lambda(1800)$, $\Sigma(1480)$, $\Sigma(1620)$ and $\Sigma(1750)$ ones. We finally argue about our preferred solution.

PACS. 11.80.-m Relativistic scattering theory – 11.80.Gw Multichannel scattering – 12.39.Fe Chiral Lagrangians – 13.75.Jz Kaon-baryon interactions

1 Introduction

The study of strangeness -1 meson-baryon dynamics comprising the $\bar{K}N$ plus coupled channels has been renewed both from the theoretical and experimental sides. Experimentally, we have new exciting data like the increasing improvement in the precision of measurement of the α line of kaonic hydrogen accomplished recently by DEAR [1], and its foreseen better determination, with an expected error of a few eV, by the DEAR/SIDDHARTA Collaboration [2]. This has established a challenge to theory in order to match such precision. In this line, ref. [3] provides an improvement over the traditional Deser formula for relating scattering at threshold with the spectroscopy of hadronic atoms [4]. This is achieved by including isospin breaking corrections to the Deser formula up to and including $\mathcal{O}(\alpha^4, (m_u - m_d)\alpha^3)$, the traditional Deser formula is $\mathcal{O}(\alpha^3)$ in this counting, where α is the fine-structure constant and m_u, m_d are the masses of the lightest quarks u and d. This is a first necessary step since the DEAR data have a precision of 20%, of the same order as the corrections worked out in ref. [3]. In addition, one needs a good scattering amplitude to be implemented in this equation. The study of strangeness -1 has a long history [5–12] within K-matrix models, dispersion relations, meson-exchange models, quark models, cloudy bag models or large N_c QCD, just to quote a few. However, in more recent years it has received a lot of attention from the application of $SU(3)$ baryon Chiral Perturbation Theory (CHPT) to this sector together with a unitarization procedure, see *e.g.*, [13–21]. Recently, ref. [3] pointed out the possible inconsistency of the DEAR measurement on kaonic hydrogen and K^-p scattering, since the unitarized CHPT results, able to reproduce the scattering data, were not in agreement with DEAR. Later on, the authors of ref. [20] insisted on this fact based on their own fits, although they only included partially the $\mathcal{O}(p^2)$ CHPT amplitudes [22]. However, the situation changed since ref. [21] as it was shown that one can obtain fits in unitary CHPT (UCHPT), including full $\mathcal{O}(p^2)$ CHPT amplitudes, which are compatible both with DEAR and with K^-p scattering data. We extend in this work the analysis of ref. [21] by including additional experimental data, recently measured with remarkable precision by the Crystal Ball Collaboration, for the reactions $K^-p \to \eta\Lambda$ [23] and $\pi^0\pi^0\Sigma^0$ [24]. The importance of including the latter data in any analysis of K^-p interactions has been singled out in ref. [25]. The study of K^-p plus coupled-channel interactions offers, from the theoretical point of view, a very challenging test ground for chiral effective field theories of QCD since one has there plenty of experimental data, Goldstone bosons dynamics and large and explicit $SU(3)$ breaking. In addition, this sector shows a very rich spectroscopy with many $I = 0$, 1 S-wave resonances that will be the object of our study as well. Apart from that, these interactions are interrelated with many other interesting areas, as listed in ref. [21], *e.g.*, possible kaon condensation in neutron-proton stars [26–29], large yields of K^- in

[a] e-mail: oller@um.es

heavy-ions collisions [30,31], kaonic atoms [32] or non-zero strangeness content of the proton [33,34].

In sect. 2 we outline the theoretical formalism employed to calculate the strong S-wave amplitudes in coupled channels. In sect. 3 we review the data and fits delivered in ref. [21] and present an $\mathcal{O}(p)$ fit to the same data. In the next section we include further data and give new fits for the prior and new data. These fits are classified in two families, particularly based on the agreement or disagreement with respect to the DEAR measurement of kaonic hydrogen. In sect. 5 we discuss the pole content and its relation with observed resonances for the most representative fits. We end with some conclusions giving reasons to fix our preferred fit.

2 Formalism

CHPT is the effective field theory of strong interactions at low energies [35–41]. In refs. [42,43] its extension to treat baryonic fields was pioneered. We concentrate here on processes including one baryon, both in the initial and final state, as well as in the intermediate ones. CHPT applied to this situation is usually called baryon CHPT. In the $SU(2)$ sector it has been very successful, see *e.g.* [37–39], and references therein. However, due to the relatively large mass of the strange quark, pure perturbative applications of $SU(3)$ baryon CHPT suffer from converging problems. Notice that while in $SU(2)$ one has m_π as an expansion parameter, for $SU(3)$ one also has m_K, with m_π, m_K the masses of pions and kaons, respectively, being the latter much larger than the former. These facts make that cancellations of large contributions at second and third chiral order often happen with still sizable $\mathcal{O}(p^4)$ contributions, see, *e.g.*, refs. [44–46]. Even more, for the case of S-wave $I = 0$ $\bar{K}N$ scattering lengths, the CHPT prediction is a disaster [44]. This is due to the presence of the $\Lambda(1405)$-resonance below and close to the $\bar{K}N$ threshold. The situation changes once the chiral expansion is implemented with a resummation of unitarity bubbles [13], showing that chiral Lagrangians can be used in strangeness -1 meson-baryon interactions reproducing this resonance. In ref. [17] the resummation of the right-hand cut or unitarity cut (taking into account unitarity and analyticity) in the CHPT expansion was systematized to any two-body process without spoiling the chiral counting and the CHPT series up to the considered order. This gives rise to the known Unitary CHPT or UCHPT. This work originated in turn from a series of previous works [14,47,48,15,16,49], where similar techniques were already employed in meson-meson and meson-baryon production and scattering.

Meson-baryon interactions are described to lowest order in the CHPT expansion, *i.e.* at $\mathcal{O}(p)$, by the chiral Lagrangian

$$\mathcal{L}_1 = \langle i\bar{B}\gamma^\mu[D_\mu, B]\rangle - m_0\langle\bar{B}B\rangle + \frac{D}{2}\langle\bar{B}\gamma^\mu\gamma_5\{u_\mu, B\}\rangle + \frac{F}{2}\langle\bar{B}\gamma^\mu\gamma_5[u_\mu, B]\rangle, \quad (2.1)$$

where m_0 stands for the octet baryon mass in the $SU(3)$ chiral limit. The trace $\langle\cdots\rangle$ runs over flavor indices and the axial-vector couplings are constrained by $F + D = g_A = 1.26$. We use $D = 0.80$ and $F = 0.46$ extracted from hyperon decays [50]. Furthermore, $u_\mu = iu^\dagger(\partial_\mu U)u^\dagger$, $U(\Phi) = u(\Phi)^2 = \exp(i\sqrt{2}\Phi/f)$, with f the pion decay constant in the $SU(3)$ chiral limit, and the covariant derivative $D_\mu = \partial_\mu + \Gamma_\mu$ with $\Gamma_\mu = [u^\dagger, \partial_\mu u]/2$. The 3×3 flavor matrices Φ and B collect the lightest octets of pseudoscalar mesons (π, K, η) and baryons $(N, \Sigma, \Lambda, \Xi)$, respectively:

$$\Phi = \begin{pmatrix} \frac{\pi^0}{\sqrt{2}} + \frac{\eta}{\sqrt{6}} & \pi^+ & K^+ \\ \pi^- & -\frac{\pi^0}{\sqrt{2}} + \frac{\eta}{\sqrt{6}} & K^0 \\ K^- & \bar{K}^0 & -\frac{2\eta}{\sqrt{6}} \end{pmatrix},$$

$$B = \begin{pmatrix} \frac{\Sigma^0}{\sqrt{2}} + \frac{\Lambda}{\sqrt{6}} & \Sigma^+ & p \\ \Sigma^- & -\frac{\Sigma^0}{\sqrt{2}} + \frac{\Lambda}{\sqrt{6}} & n \\ \Xi^- & \Xi^0 & -\frac{2\Lambda}{\sqrt{6}} \end{pmatrix}. \quad (2.2)$$

At next-to-leading order (NLO) in CHPT, *i.e.* $\mathcal{O}(p^2)$, the meson-baryon interactions are described by the Lagrangian

$$\mathcal{L}_2 = b_0\langle\bar{B}B\rangle\langle\chi_+\rangle + b_D\langle\bar{B}\{\chi_+, B\}\rangle + b_F\langle\bar{B}[\chi_+, B]\rangle + b_1\langle\bar{B}[u_\mu, [u^\mu, B]]\rangle + b_2\langle\bar{B}\{u_\mu, \{u^\mu, B\}\}\rangle + b_3\langle\bar{B}\{u_\mu, [u^\mu, B]\}\rangle + b_4\langle\bar{B}B\rangle\langle u_\mu u^\mu\rangle + \cdots . \quad (2.3)$$

Here ellipses denote terms that do not produce new independent contributions to the S-wave meson-baryon scattering at $\mathcal{O}(p^2)$. In addition, $\chi_+ = u^\dagger\chi u^\dagger + u\chi^\dagger u$, $\chi = 2B_0\mathcal{M}_q$, $\mathcal{M}_q$ is the diagonal quark mass matrix (m_u, m_d, m_s), and $B_0 f^2 = -\langle 0|\bar{q}q|0\rangle$, the quark condensate in the $SU(3)$ chiral limit. The b_i couplings present in eq. (2.3) are fitted to data, with the subscript i referring both to B, D, F as well as to 1, 2, 3, 4. Nevertheless, in the fitting process we will impose three relations to be satisfied between the b_i, hence decreasing to the same extent the number of free parameters.

From the Lagrangians of eqs. (2.1) and (2.3) we calculate the $\mathcal{O}(p)$ and $\mathcal{O}(p^2)$ meson-baryon amplitudes. The $\mathcal{O}(p)$ expressions in the canonical basis for the baryons[1] are given in ref. [17]. The $\mathcal{O}(p^2)$ expressions are given in ref. [51]. The calculated chiral amplitudes are then projected in the S-wave according to

$$T_{ji}(W) = \frac{1}{4\pi}\int \mathrm{d}\Omega\, T_{ji}(W, \Omega; \sigma, \sigma), \quad (2.4)$$

where $T_{ij}(W, \Omega; \sigma, \sigma)$ is a generic meson-baryon scattering amplitude of channel i into channel j depending on W, the total energy in the center-of-mass frame (CM), angles, Ω, and the initial and final spin of the baryons, σ, with $\sigma = \pm 1/2$. The result of eq. (2.4) does not depend on the particular sign for σ.

[1] The canonical basis is given by the fields B_a, $a = 1, \ldots, 8$, such that $B = \sum_{a=1}^{8} B_a\lambda_a/\sqrt{2}$, with λ_a the Gell-Mann matrices and B the matrix given in eq. (2.2).

We have ten meson-baryon coupled channels with strangeness −1 (or zero hypercharge): $\pi^0\Lambda$, $\pi^0\Sigma^0$, $\pi^-\Sigma^+$, $\pi^+\Sigma^-$, K^-p, $\bar{K}^0n$, $\eta\Lambda$, $\eta\Sigma^0$, $K^0\Xi^0$ and $K^+\Xi^-$, in increasing threshold energy order. Each channel is labelled by its position (1 to 10) in the previous list. We denote by ${T_\chi^{(1)}}_{ij}$ the CHPT amplitudes at $\mathcal{O}(p)$ and by ${T_\chi^{(2)}}_{ij}$ those at $\mathcal{O}(p^2)$, with the subscripts ij indicating the scattering process $i \to j$, so that a CHPT amplitude up to and including $\mathcal{O}(p^2)$ is given by ${T_\chi^{(1)}}_{ij} + {T_\chi^{(2)}}_{ij}$. We employ these perturbative amplitudes as input for UCHPT at NLO. The scheme is the following [17]. Two-body partial-wave amplitudes can be written in matrix notation as

$$T(W) = \left[I + \mathcal{T}(W)\cdot g(s)\right]^{-1}\cdot \mathcal{T}(W), \qquad (2.5)$$

with $s = W^2$, the Mandelstam s variable. The matrix elements of $T(W)$ are those of eq. (2.4). Equation (2.5) was derived in [17] by employing a coupled-channel dispersion relation for the inverse of a partial wave $T_{ij}(W)$. The unitarity or right-hand cut is taken into account easily by the discontinuity of $T^{-1}(W)|_{ij}$ for W above the i_{th} threshold, which is given by the phase space factor $-\delta_{ij}q_i/8\pi W$, with q_i the CM three-momentum of channel i. This factor is given by the imaginary part of the diagonal matrix $g(s)$, where $g(s)_i$ is the i_{th} channel unitarity bubble:

$$g(s)_i = \frac{1}{(4\pi)^2}\left\{a_i(\mu) + \log\frac{M_i^2}{\mu^2} - \frac{m_i^2 - M_i^2 + s}{2s}\log\frac{M_i^2}{m_i^2}\right.$$
$$+\frac{q_i}{W}\left[\log(s-\Delta+2Wq_i) + \log(s+\Delta+2Wq_i)\right.$$
$$\left.\left. - \log(-s+\Delta+2Wq_i) - \log(-s-\Delta+2Wq_i)\right]\right\}, \qquad (2.6)$$

here $\Delta = m_i^2 - M_i^2$ and m_i, M_i are the baryon and meson masses for channel i, respectively. In the following, μ will be fixed to the value of the ρ mass, $\mu = M_\rho \simeq 0.77\,\mathrm{GeV}$. In other terms, the $g(s)_i$ satisfy a once subtracted dispersion relation,

$$g(s)_i = g(s_0) - \frac{s-s_0}{\pi}\int_{s_{th,i}}^{\infty}\mathrm{d}s'\frac{q_i}{8\pi W'}\frac{1}{(s'-s)(s'-s_0)}\,, \qquad (2.7)$$

whose explicit expression is given above, eq. (2.6). On the other hand, $s_{th,i}$ is the value of s for the threshold of channel i. The resummation of the right-hand cut is justified in order to resum the chain of unitarity bubbles that is enhanced by the large masses of kaons and baryons. This spoils the straightforward use of the chiral series [43, 22]. The dispersion relation above is once subtracted because phase space tends to a constant for $s \to \infty$. This is why a subtraction constant $a_i(\mu)$ for each channel appears in the $g(s)_i$-function. In our problem, isospin symmetry reduces the number of subtraction constants from 10 to 6 [18], a_1, $a_2 = a_3 = a_4$, $a_5 = a_6$, a_7, a_8 and $a_9 = a_{10}$. On the other hand, we keep the physical masses of mesons and baryons in the calculation of $g(s)_i$, which then produces pronounced cusp effects. The interaction kernel $\mathcal{T}(W)$ ($\mathcal{T} = \mathcal{T}_1 + \mathcal{T}_2 + \cdots$, where subscripts indicate the chiral order), is fixed by matching (2.5) with the baryon CHPT amplitudes T_χ order by order, as clearly explained in [17]. At leading order, $\mathcal{O}(p)$, $\mathcal{T}_1 = T_\chi^{(1)}$ while at NLO, $\mathcal{O}(p^2)$, $\mathcal{T}_2 = T_\chi^{(2)}$. The matching can be done to any arbitrary order and for $\mathcal{O}(p^3)$ or higher $\mathcal{T}_n \neq T_\chi^{(n)}$. Explicit expressions for $T_\chi^{(1)} + T_\chi^{(2)}$, and hence for $\mathcal{T}_1 + \mathcal{T}_2$, are given in ref. [51]. The $\mathcal{T}$-matrix, up to and including $\mathcal{O}(p^2)$, incorporates local and pole terms as well as crossed channel dynamics contributions in the dispersion relation for T^{-1}, see fig. 1.

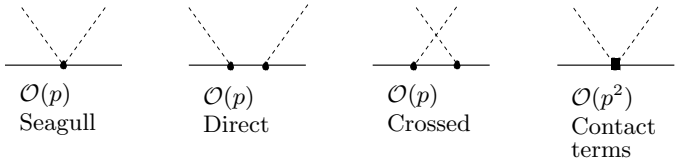

Fig. 1. Diagrams for the calculation of the baryon CHPT scattering amplitudes up to and including $\mathcal{O}(p^2)$. The first three diagrams are $\mathcal{O}(p)$ while the latest is $\mathcal{O}(p^2)$.

3 Data and fits of ref. [21]

We now discuss the data employed in ref. [21] to obtain its fits A_4^+ and B_4^+, since we are going to use the same data in our own fits. The latter include the $\sigma(K^-p \to K^-p)$ elastic cross-section [52–55], the $\sigma(K^-p \to \bar{K}^0n)$ charge exchange one [52,53,55–57], and several hyperon production reactions, $\sigma(K^-p \to \pi^+\Sigma^-)$ [52–54], $\sigma(K^-p \to \pi^-\Sigma^+)$ [53–55], $\sigma(K^-p \to \pi^0\Sigma^0)$ [53] and $\sigma(K^-p \to \pi^0\Lambda)$ [53]. In our normalization the corresponding cross-section, keeping only the S-wave, is given by

$$\sigma(K^-p \to MB) = \frac{1}{16\pi s}\frac{p'}{p}\,|T_{K^-p\to MB}|^2, \qquad (3.1)$$

where MB denotes the final meson-baryon system, p' the final CM three-momentum and p the initial one.

In addition, we also fit the precisely measured ratios at the K^-p threshold [58,59]:

$$\gamma = \frac{\sigma(K^-p\to\pi^+\Sigma^-)}{\sigma(K^-p\to\pi^-\Sigma^+)} = 2.36\pm0.04,$$
$$R_c = \frac{\sigma(K^-p\to\text{charged particles})}{\sigma(K^-p\to\text{all})} = 0.664\pm0.011, \qquad (3.2)$$
$$R_n = \frac{\sigma(K^-p\to\pi^0\Lambda)}{\sigma(K^-p\to\text{all neutral states})} = 0.189\pm0.015.$$

The first two ratios, which are Coulomb corrected, are measured with 1.7% precision, which is of the same order as the expected isospin violations. Indeed, all the other observables we fit have uncertainties larger than 5%.

Since we are just considering the S-wave partial waves, we only include in the fits those data points for the several K^-p cross-sections with laboratory frame K^-

three-momentum $p_K \leq 0.2\,\mathrm{GeV}$. This also enhances the sensitivity to the lowest-energy region in which we are particularly interested. We also include in the fits the $\pi^\pm\Sigma^\mp$ event distributions from the chain of reactions $K^-p \to \Sigma^+(1660)\pi^-$, $\Sigma^+(1660) \to \pi^+\Sigma\pi$ [60]. The $\Sigma^+\pi^-$ and $\Sigma^-\pi^+$ have $I = 1$ Clebsch-Gordan coefficients opposed in sign while both have the same $I = 0$ Clebsch-Gordan coefficient. Since this process is dominated by the $\Lambda(1405)$-resonance, which afterwards decays into $\Sigma\pi$, we want to remove as much as possible the $I = 1$ contamination. Indeed, one can observe small differences in the data [60] between the event distributions for $\Sigma^\pm\pi^\mp$ due to this $I = 1$ effect, that indeed is enhanced by the presence of $I = 1$ resonances close to the $\Lambda(1405)$ energy region, as reported in [17,18] or within the entry $\Sigma(1480)$ of the PDG [61], qualified there as bumps. See also ref. [62] for a possible recent observation of this resonance. No $I = 1$ resonance around the $\bar{K}N$ threshold is reported in refs. [19,63,64]. We shall present our own results on that in sect. 5, dedicated to spectroscopy. In order to remove the interference with the $I = 1$ contribution we take the average between the $\Sigma^\pm\pi^\mp$ event distributions. For the calculation we follow [17], where a generic $L = I = 0$ source is taken for the generation of the final $\Sigma^\pm\pi^\mp$ particles, L is the angular momentum. Final-state interactions are taken into account in the very same way as for the strong meson-baryon scattering amplitudes. In this case, the "production" vertices for the i_{th} channel are the $\mathcal{T}_{\alpha i}$ matrix elements, from the "source"$\equiv \alpha_{th}$ channel. Afterwards, final-state interactions give rise to the factor $[I + K \cdot g]^{-1}$. Hence, the elementary production vertices, R_i, because of final-state interactions, change to $R \to [I + \mathcal{T}] \cdot R = F$, with F_i the transition amplitude to the i_{th} channel. In order to simplify matters, as done as well in ref. [17], we only consider $R_i \neq 0$ for the $\bar{K}N$ and $\pi\Sigma$ channels, as they are the only channels with $I = 0$ component that open in the considered energy region around the $\Lambda(1405)$. Any other channels with $I = 0$ component are much higher in energy. Hence, $R_i = (0, r, r, r, r', r', 0, 0, 0, 0)$. The final expression considered is then

$$\frac{\mathrm{d}N_{\pi\Sigma}}{\mathrm{d}W} = \left| r(D_{32} + D_{33} + D_{34}) + r'(D_{35} + D_{36}) \right|^2 p_{\pi^-\Sigma^+}, \tag{3.3}$$

with $D = [I + \mathcal{T} \cdot g]^{-1}$. In this way, the $I = 0$ component is the only one contributing. We have taken in eq. (3.3) the $\pi^-\Sigma^+$ channel to evaluate the three-momentum $p_{\pi^-\Sigma^+}$. We could have also taken the $\pi^+\Sigma^-$, being the numerical effects negligible. The parameters r and r' are fitted to the average of the $\pi^\pm\Sigma^\mp$ event distribution data.

The number of data points included in each fit, without the data for the energy shift and width of kaonic hydrogen, is 97. Unless the opposite is stated, we also include in the fits the DEAR measurement of the shift and width of the $1s$ kaonic hydrogen energy level [1],

$$\begin{aligned} \Delta E &= 193 \pm 37(\mathrm{stat}) \pm 6(\mathrm{syst.})\,\mathrm{eV}, \\ \Gamma &= 249 \pm 111(\mathrm{stat.}) \pm 39(\mathrm{syst.})\,\mathrm{eV}, \end{aligned} \tag{3.4}$$

which is around a factor two more precise than the KEK [65] previous measurement, $\Delta E = 323 \pm 63 \pm 11\,\mathrm{eV}$ and $\Gamma = 407 \pm 208 \pm 100\,\mathrm{eV}$. To calculate the shift and width of the $1s$ kaonic hydrogen state we use the results of [3] incorporating isospin breaking corrections up to and including $\mathcal{O}(\alpha^4, (m_d - m_u)\alpha^3)$. The final expression taken from ref. [3] is

$$T^{(0)}_{KN} = 4\pi \left(1 + \frac{M_{K^+}}{m_p}\right) \frac{(a_0 + a_1)/2 + q_0 a_0 a_1}{1 + q_0(a_0 + a_1)/2}\,,$$

$$\Delta E - \frac{i}{2}\Gamma = -\frac{\alpha^3\mu_c^3}{2\pi M_{K^+}}\, T^{(0)}_{KN} \left\{1 - \frac{\alpha\mu_c s_1(\alpha)}{4\pi M_{K^+}} T^{(0)}_{KN}\right\}, \tag{3.5}$$

where, as suggested in that reference, we have taken for practical purposes δT_{KN}, $\delta_1^{vac} = 0$. The notation followed is that of ref. [3]. We have displayed these formulas in order to show how the strong $\bar{K}N$ scattering lengths in the isospin limit, a_0 and a_1 for $I = 0$, 1, respectively, enter in eq. (3.5). The definition of the isospin limit is the same as in ref. [3], taking for the mass of the K, π and nucleon multiplets that of the positively charged particle. We compare the results obtained from eq. (3.5) with those from the Deser formula [4], directly given in terms of the K^-p scattering length, a_{K^-p}, $\Delta E - i\,\Gamma/2 = -2\alpha^3\mu_c^2 a_{K^-p}$, without considering the isospin limit. Within the uncertainties given in ref. [3], one can use $4\pi(1+M_{K^+}/m_p)a_{K^-p}$ instead of $T^{(0)}_{KN}$ in eq. (3.5). We have checked that for all our fits the resulting ΔE and Γ are very close to those obtained directly employing eq. (3.5). Hence we do not elaborate more on this point.

We further constrain our fits by computing at $\mathcal{O}(p^2)$ in baryon $SU(3)$ CHPT several πN observables with the values of the low-energy constants involved in the fit. Unitarity corrections in the πN sector are not as large as in the $S = -1$ sector, *e.g.*, there is no something like a $\Lambda(1405)$ resonance close to threshold, and hence a calculation within pure $SU(3)$ baryon CHPT is more reliable for this sector. Thus, we calculate at $\mathcal{O}(p^2)$, a^+_{0+}, the isospin-even pion-nucleon S-wave scattering length, $\sigma_{\pi N}$, the pion-nucleon σ term, and m_0 from the value of the proton mass m_p,

$$\begin{aligned} \sigma_{\pi N} &= -2m_\pi^2(2b_0 + b_D + b_F), \\ a^+_{0+} &= -\frac{m_\pi^4}{2\pi f^2}\left[(2b_0 + b_D + b_F) - (b_1 + b_2 + b_3 + 2b_4) + \frac{g_A^2}{8m_p}\right], \\ m_p &= m_0 - 4m_K^2(b_0 + b_D - b_F) - 2m_\pi^2(b_0 + 2b_F). \end{aligned} \tag{3.6}$$

We do not consider the isospin-odd πN scattering length a^-_{0+} since up to $\mathcal{O}(p^2)$ it is independent of the low-energy constants b_i [66]. The $\sigma_{\pi N}$ term receives sizable higher-order corrections from the mesonic cloud which are expected to be positive and around 10 MeV [67]. Since we evaluate it just at $\mathcal{O}(p^2)$, we enforce $\sigma_{\pi N} = 20$, 30 or 40 MeV in the fits ($\sigma_{\pi N} = 45 \pm 8\,\mathrm{MeV}$ [68]). For the same reason, $m_0 = 0.7$ or 0.8 GeV was enforced in ref. [21] ($m_0 = 0.77 \pm 0.11\,\mathrm{GeV}$ from ref. [45] or $0.71 \lesssim m_0 \lesssim 1.07\,\mathrm{GeV}$ [69]). In the new fits to be discussed in the next section, we use $m_0 = 0.9 \pm 0.2$, as suggested by ref. [69]. We also include the value $a^+_{0+} = -(1 \pm 1) \cdot 10^{-2}\, m_\pi^{-1}$ in the fit procedure. This value results after considering its experimental measurement [70], $a^+_{0+} = -(0.25 \pm 0.49) \cdot 10^{-2}\, m_\pi^{-1}$,

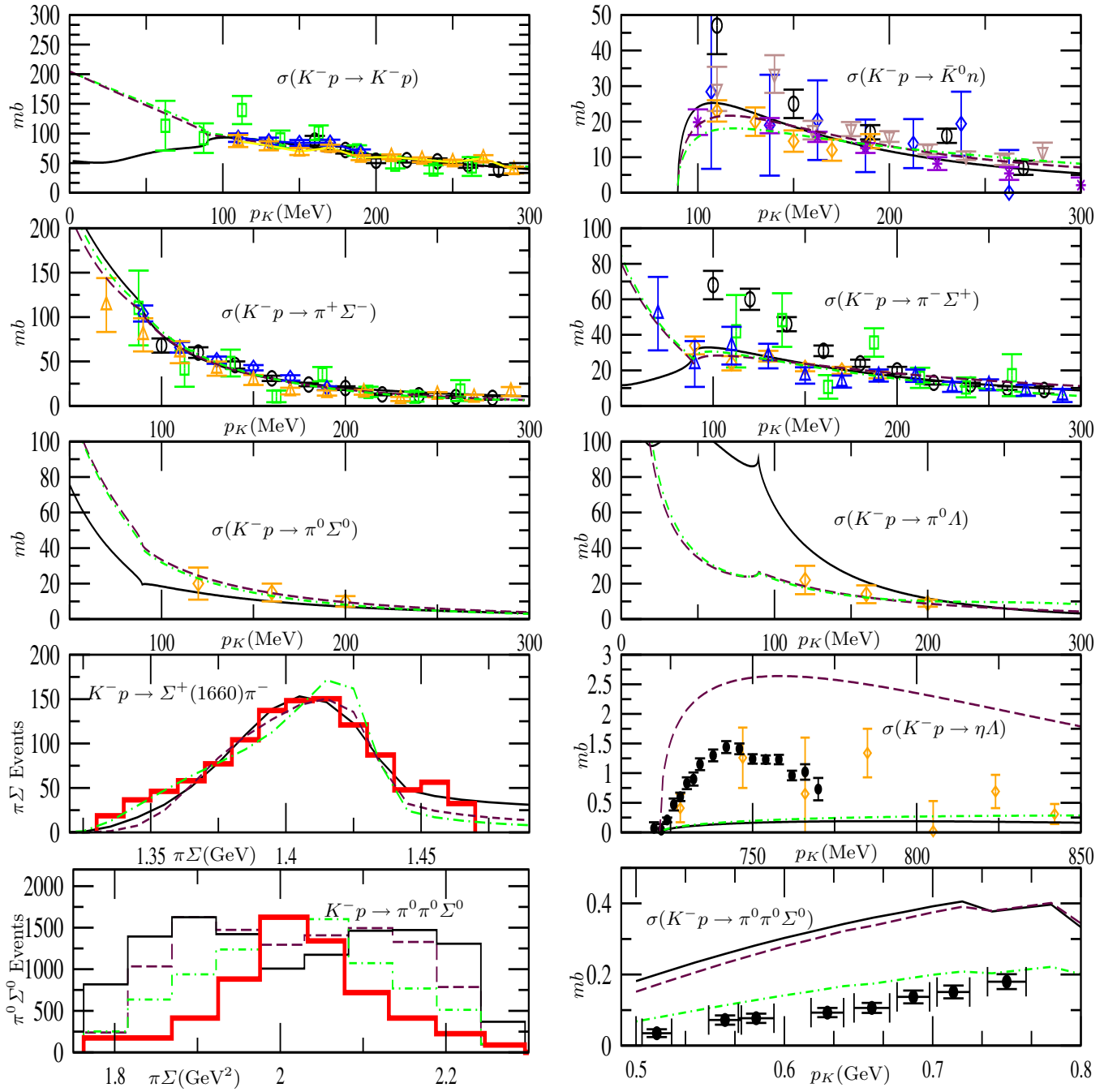

Fig. 2. The solid lines correspond to the fit A_4^+, the dashed ones to B_4^+ and the dash-dotted lines to the $\mathcal{O}(p)$ fit given in table 1. The data employed in the fit is that of sect. 3. The experimental references for the first six panels are: squares [52], diamonds [53], upwards triangles [54], circles [55], stars [56] and downwards triangles [57]. The data in the seventh panel, thick solid line, are from ref. [60]. The circles and diamonds in the eighth panel are from refs. [23,71], in order. The thick solid line in the ninth panel is the experimental data [24]. While the data of the tenth panel correspond to ref. [24].

and the theoretical expectation of positive $\mathcal{O}(p^3)$ corrections around $+1\cdot 10^{-2}\, m_\pi^{-1}$ from unitarity [66]. Thus, the inclusion of eq. (3.6) implies three relations between the b_i that basically reduce by three[2] the number of fitted parameters shown in tables 1, 3 and 5. It is worth stressing that for all the fits we minimize strictly the χ^2, that is, each data point is weighted according to its experimental error. We do not include the data from ref. [55] in the $\sigma(K^-p\to\pi^-\Sigma^+)$ cross-section since they are incompatible with all the other data.

[2] Here "basically" is because $a_{0^+}^+$ and m_0 are given with some error, while $\sigma_{\pi N}$ is fixed.

Table 1. Resulting values for the parameters of the fits A_4^+, third column, and B_4^+, fourth column. The $\mathcal{O}(p)$ fit is given in the fifth column. The fits A_4^+ and B_4^+ are from ref. [21]. In the last column the asterisks mean that the corresponding parameters are fixed to 0 since it is an $\mathcal{O}(p)$ calculation.

Units		A_4^+	B_4^+	$\mathcal{O}(p)$
MeV	f	79.8	89.2	88.0
GeV^{-1}	b_0	-0.855	-0.318	0^*
GeV^{-1}	b_D	$+0.715$	-0.101	0^*
GeV^{-1}	b_F	-0.036	-0.314	0^*
GeV^{-1}	b_1	$+0.605$	-0.193	0^*
GeV^{-1}	b_2	$+1.075$	-0.275	0^*
GeV^{-1}	b_3	-0.189	-0.153	0^*
GeV^{-1}	b_4	-1.249	-0.277	0^*
	a_1	-1.155	-1.570	-0.472
	a_2	-0.383	-2.062	-1.572
	a_5	-1.304	-2.605	-1.266
	a_7	-1.519	-1.568	-1.853
	a_8	-1.212	-2.064	-1.210
	a_9	-0.145	-0.886	$+3.337$

In fig. 2 we show the scattering data and the $\pi\Sigma$ event distributions in the first seven panels, from left to right and top to bottom. The solid and dashed curves, correspond to the A_4^+ and B_4^+ fits, respectively. They reproduce well the data included in the fits of ref. [21] and discussed in this section. The last three panels in the same figure correspond to other data not considered in the present fits nor in ref. [21]. In the eighth panel we show the total cross-section $\sigma(K^-p \to \eta\Lambda)$. The solid points come from ref. [23] while the diamonds are much older [71]. The $\pi^0\Sigma^0$ event distribution and the total cross section for the reaction $K^-p \to \pi^0\pi^0\Sigma^0$, measured in [24], are displayed, respectively, in the ninth and tenth panels. The data in the last three panels will be presented and discussed further in the next section. It is clear from the figure that the A_4^+ and B_4^+ fits do not reproduce adequately the data in the last three panels. In fig. 2, we also show by the dash-dotted lines the $\mathcal{O}(p)$ fit to the same data. As we see, this fit, with 4 free parameters less than the others[3], is able to reproduce the scattering data but fails as well in the reproduction of $\sigma(K^-p \to \eta\Lambda)$, although its disagreement with the data from the reaction $K^-p \to \pi^0\pi^0\Sigma^0$ [24] is neatly smaller than for the fits A_4^+ and B_4^+. In table 1 we give the values of the fitted parameters. We show in table 2 the resulting values for the ratios of eq. (3.2) and observe that for all the fits there is agreement with experiment for γ and R_n within the small errors given. For R_c, the fits B_4^+ and $\mathcal{O}(p)$ agree within the experimental error, while A_4^+ agrees with the experimental value at the level of 5%, which is equally satisfactory since we do not intend at this stage to arrive at such precision in the description of strong interactions in this sector, where even isospin breaking corrections should be systematically included. We also show in the same table the kaonic hydrogen data included in the fit, as well as other magnitudes as explained in the table caption. Only the A_4^+ fit is in agreement with the shift and width of kaonic hydrogen from DEAR [1]. The fits B_4^+ and $\mathcal{O}(p)$ are in agreement with KEK [65] but disagrees with DEAR [1]. We also show the calculated energy shift and width of kaonic hydrogen from the Deser formula. The differences with respect to the results from the more elaborated eq. (3.5) are huge for Γ in the fits B_4^+ and $\mathcal{O}(p)$ and by far much smaller, a correction of just a few percent, in the fit A_4^+. For the $\mathcal{O}(p)$ fit the value for a_9 is quite large, although this parameter turns out with very large errors as given by the minimizing subroutine [72]. Indeed, its upper error is much larger than the value of the parameter itself. Hence one concludes that this parameter is left undetermined by the $\mathcal{O}(p)$ fit. We should also remark that all the parameters in table 1 are of natural size. The b_i are of order GeV^{-1} and the $|a_i|$ are around 1. This is the natural size for the a_i since from the value of the imaginary part of $g(s)_i$ above threshold, $-q_i/8\pi W$, multiplying it by $16\pi^2$, the prefactor in eq. (2.6), one has $-q_i/2\pi W$. Taking for W the mass of a nucleon, m_N, the ratio is then the quotient of q_i over $\simeq 150$ MeV, which is typically a quantity of order 1. Furthermore, from the unitarity corrections to the chiral series induced by $g(s)$, which start at $\mathcal{O}(p^3)$, one can derive the scale $\Lambda_U \simeq 16\pi^2 f^2/2m_N|a_i|$. Again this scale is of natural size, around the mass of the ρ, for $|a_i| = 1$. However, for larger values of $|a_i|$ it can be quite small, *e.g.*, of the order of the difference between the masses of the nucleon and $\Delta(1232)$. Regarding the precise values for b_0, b_D and b_F we can compare our values in table 1 with the determination based on resonance saturation and reproduction of the masses of the lightest baryon octet and $\sigma_{\pi N}$ from ref. [45]. The authors of ref. [45] conclude that $b_0 \simeq -0.61$, $b_D \simeq 0.08$ and $b_F \simeq -0.32$ in units of GeV^{-1}. From a pure $\mathcal{O}(p^2)$ analysis of baryon masses and $\sigma_{\pi N}$ one has, in the same units, $b_D = 0.064$, $b_F = -0.209$ and $b_0 = -0.518$ or -0.807, depending on whether the value for $\sigma_{\pi N}$ is taken from ref. [68] or from ref. [34], respectively. These values look somewhat closer to those of the fit B_4^+ than to the values of the fit A_4^+. However, the comparison is not straightforward since we employ the $\mathcal{O}(p^2)$ couplings in UCHPT, which resums large contributions in this sector, so that there is no reason why the values should be the same as in CHPT. It is remarkable that the value for b_3 is very similar both in the fits A_4^+ and B_4^+. Indeed, from ref. [45] one also has $b_1 = -0.004$, $b_2 = +0.018$, $b_3 = -0.187$ and $b_4 = -0.109$, hence the value for b_3 is quite similar also to those in table 1. Finally, in ref. [13] a value of around $-0.15\,\mathrm{GeV}^{-1}$ was given as well and in many of the fits of ref. [20] values around $-0.2\,\mathrm{GeV}^{-1}$ are reported. In the fits that we present later, b_3 mostly appear between -0.2 and $-0.3\,\mathrm{GeV}^{-1}$.

[3] We recall that in the $\mathcal{O}(p^2)$ fits we also consider m_0, $\sigma_{\pi N}$ and $a_{0^+}^+$, directly given by eqs. (3.6) in terms of the low-energy constants b_i. In this way, although there are 7 low-energy constants only four are really kept as free parameters in the $\mathcal{O}(p^2)$ fits. This statement, however, is only approximate because neither m_0 nor $a_{0^+}^+$ are exactly sticked to a value, $m_0 = 0.9 \pm 0.2\,\mathrm{GeV}$ and $a_{0^+}^+ = -(1 \pm 1)10^{-2}$.

Table 2. Values for the ratios at threshold of eq. (3.2), energy shift (ΔE) and width (Γ) of the ground state of the kaonic hydrogen, both using eq. (3.5) and the Deser formula, the latter indicated by the subscript D. We also give the K^-p S-wave scattering length, a_{K^-p}, $I=0$ and 1 $\bar{K}N$ scattering lengths in the isospin limit, a_0 and a_1, respectively, the difference between the P- and S-wave $\pi\Lambda$ phase shifts at the Ξ^- mass, $\delta_{\pi\Lambda}(\Xi)$, the lightest baryon mass in the chiral limit, m_0, the isospin even πN scattering length, a^+_{0+}, and the enforced $\sigma_{\pi N}=40^*$ MeV for the $\mathcal{O}(p^2)$ fits.

	A_4^+	B_4^+	$\mathcal{O}(p)$
γ	2.36	2.36	2.35
R_c	0.628	0.655	0.667
R_n	0.172	0.195	0.205
ΔE (eV)	201	403	390
Γ (eV)	338	477	525
ΔE_D (eV)	209	416	394
Γ_D (eV)	346	662	716
a_{K^-p} (fm)	$-0.51+i\,0.42$	$-1.01+i\,0.80$	$-0.96+i\,0.87$
a_0 (fm)	$-1.23+i\,0.45$	$-1.63+i\,0.81$	$-1.55+i\,0.87$
a_1 (fm)	$0.98+i\,0.35$	$-0.01+i\,0.54$	$-0.03+i\,0.65$
$\delta_{\pi\Lambda}(\Xi)$ (°)	2.5	0.2	−1.9
m_0 (GeV)	0.8^*	0.8^*	...
a^+_{0+} ($10^{-2}\cdot M_\pi^{-1}$)	−1.2	−1.7	...
$\sigma_{\pi N}$ (MeV)	40^*	40^*	...

The discrepancy commented of the A_4^+ and B_4^+ fits with the data not included in ref. [21], corresponding to the last three panels of fig. 2, leads us to consider new fits that include these new data from the beginning.

4 New fits with additional recent data

In addition to the data set described in sect. 3, we now include in the fits the following data, already shown in the last three panels of fig. 2:

i) The $\sigma(K^-p\to\eta\Lambda)$ cross-section was measured accurately in ref. [23] from threshold up to around $p_K=770\,\mathrm{MeV}$ ($\sqrt{s}=1.69\,\mathrm{GeV}$), with p_K the kaon three-momentum in the laboratory frame. These are 17 data points with small error bars as shown by the circles in the eighth panel of the result figures, namely, figs. 2, 4, 5. We also consider older data on this reaction [71] from $p_K=728$ up to 934 MeV ($\sqrt{s}=1.76\,\mathrm{GeV}$). They are much less precise than the previous data and up to $p_K=0.85\,\mathrm{GeV}$ are shown in the eighth panel of the same figures. Both data sets include a total of 29 new points.

ii) Data from the reaction $K^-p\to\Sigma^0\pi^0\pi^0$ recently measured in ref. [24]. These data comprise the $\pi^0\Sigma^0$ event distribution, shown in the ninth panel of the result figures by the thick solid line, and measurements of the associated total cross-section, given by the circles in the tenth panel of the same figures. The measurement of the cross-section is quite accurate, as one can see from these figures, with p_K from 0.5 GeV up to 0.75 GeV. The error bars given are calculated from ref. [24] by adding in quadrature the statistical errors (explicitly given in the paper) and a systematic error of 10% (the upper bound estimated in this reference for this source of error). These data constitute 18 demanding new points[4].

iii) Finally, we also include the recently measured difference between the P- and S-wave $\pi\Lambda$ phase shifts at the Ξ^- mass, from the determination of the $\Xi^-\to\Lambda\pi^-$ decay parameters. The results are $\delta_P-\delta_S=(4.6\pm1.4\pm1.2)^\circ$ [73] and $(3.2\pm5.3\pm0.7)^\circ$ [74]. Neglecting the tiny P-wave phase shift [75], this quantity just corresponds to $-\delta_S$. As already given in ref. [21], we obtain for this quantity 2.5° for the fit A_4^+ and 0.2° for the fit B_4^+. For the $\mathcal{O}(p)$ fit one has −1.9°, see table 2. Hence, the fit A_4^+ is the only one in agreement with the measurement at the level of one σ. In the following, we denote by $\delta_{\pi\Lambda}(\Xi)$ this phase shift difference.

Thus, in total we have 153 "scattering" data points while in ref. [21] the number of "scattering" data points, 97, was significantly smaller.

We follow a similar strategy as in the fits of [21] and then consider fits constrained to give $\sigma_{\pi N}=20$, 30 and 40 MeV. On the other hand, $m_0=0.9\pm0.2$ is included in the fits, where the range of values is taken from ref. [69], and is compatible as well with that of ref. [45]. Other works on baryon masses from baryon CHPT, in some or other variant, are [76–79].

The reaction $K^-p\to\eta\Lambda$, accurately measured by the Crystal Ball Collaboration [23], was also considered in refs. [80,63,81], where it was assumed to proceed in S-wave. This assumption is well suited since the data from ref. [23] is close to threshold and hence the S-wave should dominate, this is also indicated by the angular distributions [23]. We follow here this assumption as well and thus the strong $K^-p\to\eta\Lambda$ amplitude will be taken in S-wave.

[4] I warmly acknowledge E. Oset for having stressed to me the importance of these new data.

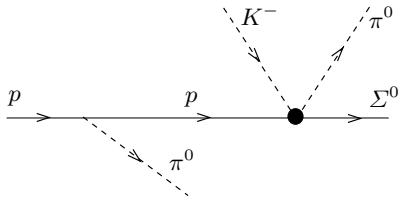

Fig. 3. Production process for the $K^-p \to \pi^0\pi^0\Sigma^0$ reaction.

According to our normalization we have

$$\sigma(K^-p \to \eta\Lambda) = \frac{1}{16\pi\, s}\,\frac{p'}{p}\,\left|T_{K^-p\to\eta\Lambda}\right|^2, \qquad (4.1)$$

as in eq. (3.1), with p' the CM three-momentum of the $\eta\Lambda$ system and p that of the initial K^-p state.

For the calculation of the $\Sigma^0\pi^0$ event distribution and the total cross-section of the reaction $K^-p \to \pi^0\pi^0\Sigma^0$, we follow the scheme of ref. [25], although we use fully relativistic amplitudes. In ref. [25] several production mechanisms for the final $\pi^0\pi^0\Sigma^0$ state are included and discussed in connection to the related process $\pi^-p \to K^0\pi\Sigma$, studied in ref. [82]. Interestingly, all of them are negligible compared with the diagram shown in fig. 3. The thick dot at the right of the figure means that the *full* $K^-p \to \pi^0\Sigma^0$ S-wave is used. Here we are assuming that the process is dominated by the S-wave meson-baryon amplitude, which is justified since we are close to the threshold of the reaction, see the last panel of figs. 2, 4 or 5. This diagram is so much enhanced compared with other possible ones [25] due to the almost on-shell character of the intermediate proton. As said above, we have recalculated this diagram in a fully Lorentz covariant way, as also done with the interaction kernel for our S-wave amplitudes. Numerically these relativistic corrections do not affect appreciably the results as compared with the non-relativistic limit taken in ref. [25]. Had the emitted meson been a kaon, things would have been different, since then large factors of M_K/m_p would have appeared. The finding of ref. [25], concerning the dominance of the diagram of fig. 3 compared with any other mechanism considered, makes us confident about the reliability of the approach and, hence, we include this reaction in our data set.

Our final expression for the reaction $K^-p \to \pi^0\pi^0\Sigma^0$ is

$$\begin{aligned} t_{\beta\alpha} = {} & \frac{D+F}{2f}\,\frac{i\,A_pA_Q}{(p-q_1)^2-m_p^2}\chi_\beta \\ & \times\Bigg\{\vec{p}\,\vec{\sigma}\left[\frac{q_1^0}{(E_p+m_p)}+\frac{q_1^0}{E_Q+m_p}+\frac{\vec{q}_1^{\,2}-2\vec{p}\,\vec{q}_1}{(E_p+m_p)(E_Q+m_p)}\right] \\ & -\vec{q}_1\vec{\sigma}\left[1+\frac{q_1^0}{E_Q+m_p}-\frac{\vec{p}^{\,2}}{(E_p+m_p)(E_Q+m_p)}\right] \\ & \times T_{K^-p\to\pi^0\Sigma^0}(W_{13})+(q_1\leftrightarrow q_2)\Bigg\}\chi_\alpha. \end{aligned} \qquad (4.2)$$

In the previous equation, $Q = p - q_1$ and p, q_1 and q_2 are the four-momenta of the incoming proton and outgoing pions, respectively, and W_{13} is CM energy of the Σ^0 and the second pion. The subscripts α and β refer to the spins of the proton and Σ^0, in order. The χ_i are Pauli spinors, $A_p = \sqrt{m_p + E_p}$ and $A_Q = \sqrt{m_p + E_Q}$, with E_q the proton energy for three-momentum $\vec{q}$, $E_q = \sqrt{m_p^2 + \vec{q}^{\,2}}$. The exchange $(q_1 \leftrightarrow q_2)$ in the end of eq. (4.2) guarantees the indistinguishableness of the two emitted neutral pions. This is the source of a major background for the $\Lambda(1405)$-resonance shape in the event distribution that makes the $\Lambda(1405)$-resonance to appear wider. Taking into account the phase space for the three final particles we have the following expression for the cross-section:

$$\begin{aligned} \sigma(K^-p \to \pi^0\pi^0\Sigma^0) = {} & \frac{1/2}{1024\, s\,\pi^5} \\ & \times \int \mathrm{d}\cos\theta_{p'}\,\mathrm{d}\phi_{p'}\,\mathrm{d}\phi_3\,\mathrm{d}m_{23}^2\,\mathrm{d}m_{12}^2\,\frac{1}{2}\sum_{\alpha,\beta=1}^{2}|t_{\alpha\beta}|^2, \end{aligned} \qquad (4.3)$$

where p' is the four-momentum of the Σ^0, ϕ_3 the azimuthal angle of the second pion, m_{12} the invariant mass of the Σ^0 and the first π^0, while m_{23} is that of the two pions. The symmetry factor 1/2 for the calculation of the total cross-sections, due to the identical neutral pions, is explicitly shown. In the calculation of the event distribution it should be removed, but since the latter is not normalized we show it for both calculations. Incidentally, we also mention that the S-wave amplitude appearing in eq. (4.2) is evaluated in the K^--(intermediate p) CM frame, which is not the CM of the whole process, in which eq. (4.3) is expressed. We have worked out the corresponding Wigner rotation matrices to calculate the scattering amplitudes in the global CM frame from the S-wave in the K^--(intermediate p) CM frame. But, since their numerical effects are negligible, we refrain from including them and giving further details about their calculation.

Table 3. Fits, presented in sect. 4.1, that agree with the DEAR data, eq. (3.4). The $\sigma_{\pi N}$ value enforced in the fits is given in the first row.

Units	$\sigma_{\pi N}$ MeV	20^*	30^*	40^*
MeV	f	75.2	71.8	67.8
GeV^{-1}	b_0	−0.615	−0.750	−0.884
GeV^{-1}	b_D	+0.818	+0.848	+0.873
GeV^{-1}	b_F	−0.114	−0.130	−0.138
GeV^{-1}	b_1	+0.660	+0.670	+0.676
GeV^{-1}	b_2	+1.144	+1.169	+1.189
GeV^{-1}	b_3	−0.297	−0.316	−0.315
GeV^{-1}	b_4	−1.048	−1.181	−1.307
	a_1	−1.786	−1.591	−1.413
	a_2	−0.519	−0.454	−0.386
	a_5	−1.185	−1.170	−1.156
	a_7	−5.251	−5.209	−5.123
	a_8	−1.316	−1.310	−1.308
	a_9	−1.186	−1.132	−1.050

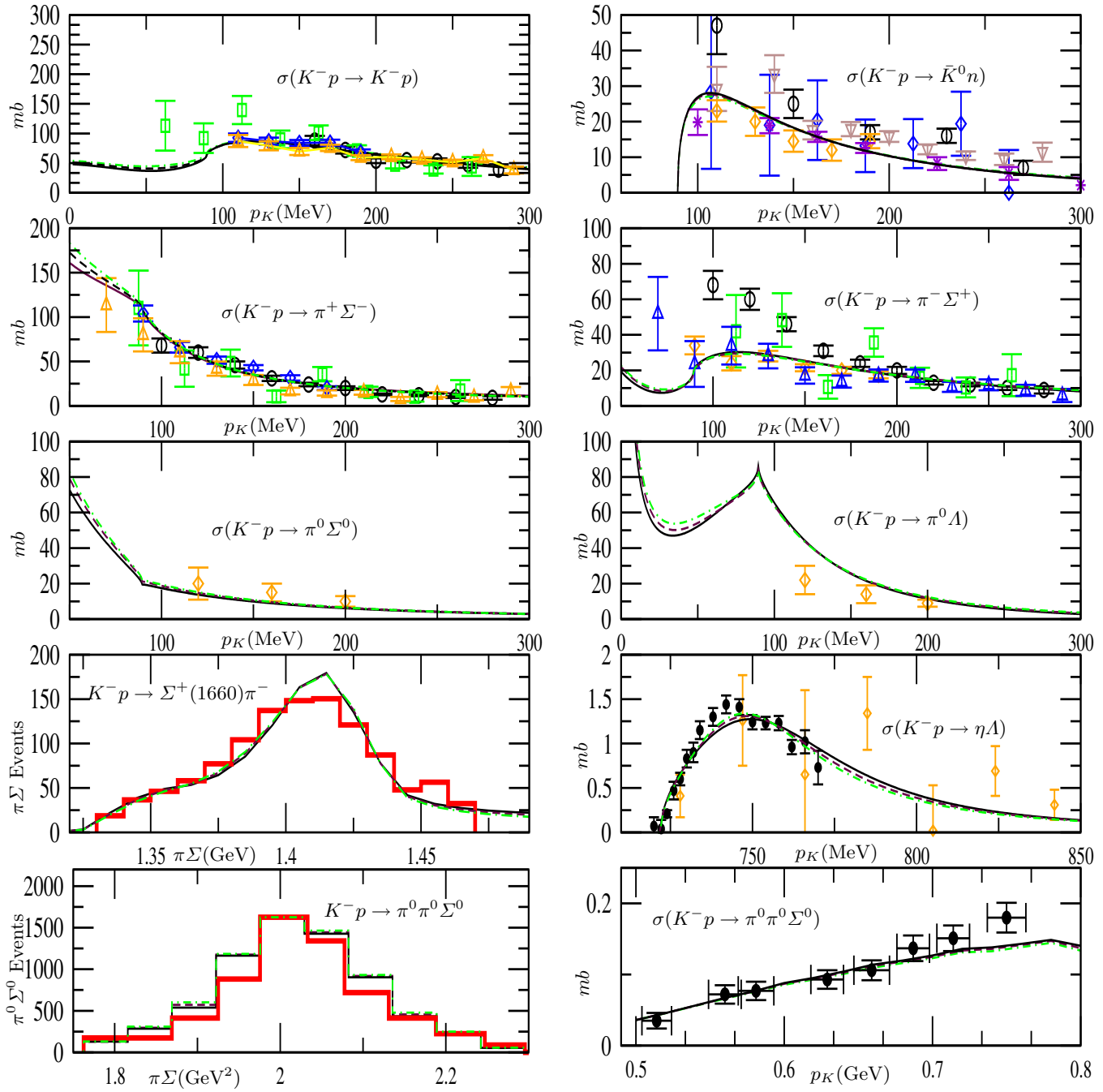

Fig. 4. The solid lines correspond to the $\sigma = 40^*$ MeV fit, the dashed lines to the 30^* MeV fit, and the dash-dotted curves to the 20^* MeV one of table 3. The different lines can be barely distinguished. For experimental references see the caption of fig. 2.

4.1 New A-type fits

We first discuss those fits that reproduce the DEAR accurate measurement, eq. (3.4), of the width and shift of kaonic hydrogen, together with the rest of data. We show in fig. 4 the reproduction of the scattering data for these new fits, that include the additional data discussed in this section. We distinguish the fits according to the enforced $\sigma_{\pi N}$ value introduced in the fit and calculated from eq. (3.6). These values, in MeV, are 40^* (solid), 30^* (dashed) and 20^* (dash-dotted lines). These fits, once the new data is included, originate from the A_4^+ one, and many fitted values of the parameters, shown in table 3, are quite similar to those of A_4^+ given in table 1. The main difference is the value for a_7 concerning the $\eta\Lambda$ channel, that is much smaller now than it was in table 1. The value for f is also a few MeV smaller now than for A_4^+. We have also tested another fit with $\sigma_{\pi N} = 45 \pm 18$ MeV, taking for $\sigma_{\pi N}$ the central value from ref. [68] and adding linearly the error given in this reference and the expected

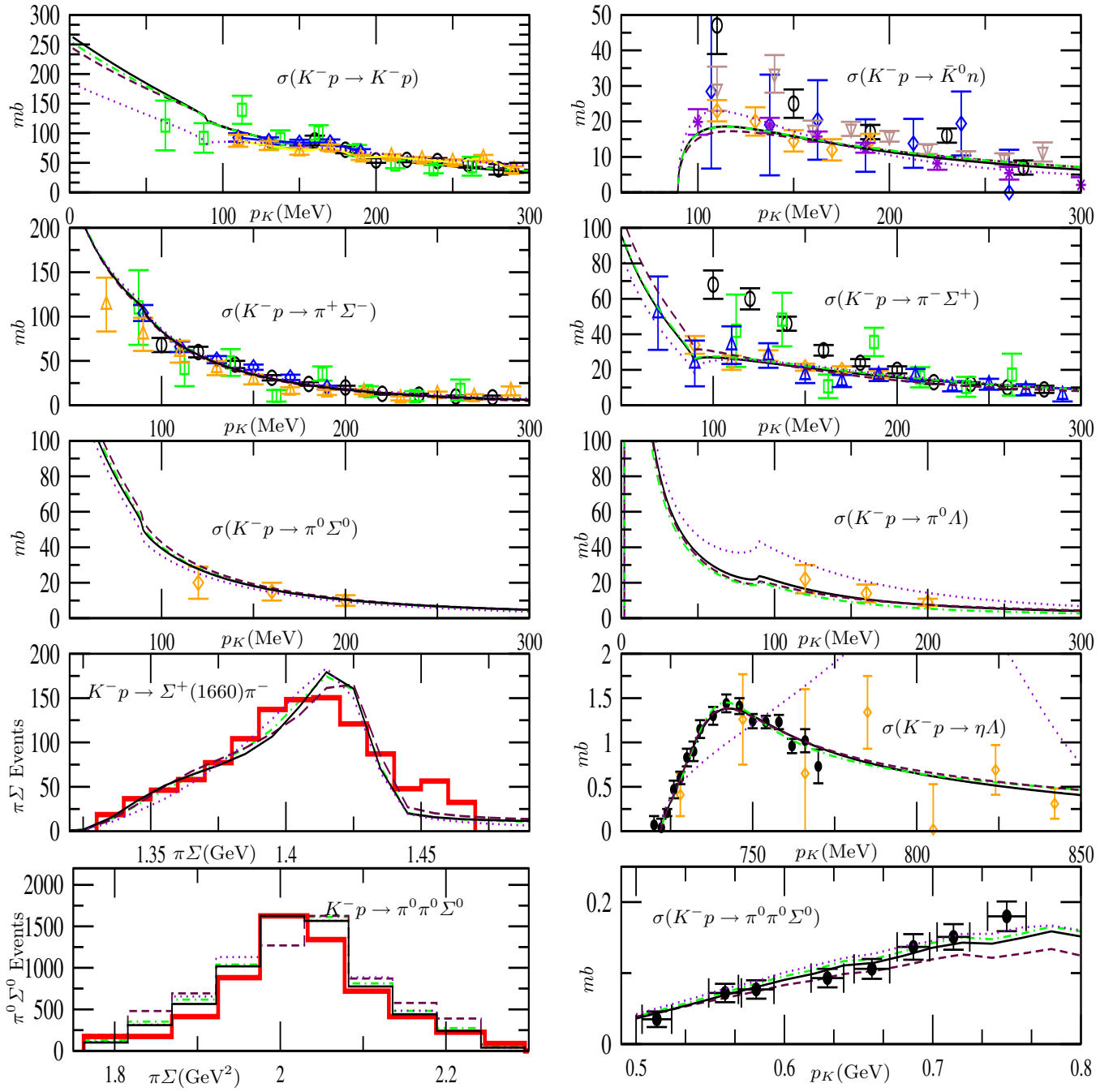

Fig. 5. The solid lines correspond to the $\sigma_{\pi N} = 40^*$ MeV fit, the dashes lines to the 30^* MeV fit, the dash-dotted curves to the 20^* MeV one and the dotted lines to the $\mathcal{O}(p)$ fit of table 5.

uncertainties from higher orders [67]. Nonetheless, the resulting fit is somehow intermediate between the fits with $\sigma_{\pi N} = 20^*$ and 30^* and we do not consider it any further. We obtain a good reproduction of the scattering data as shown in fig. 4. Although the different lines in this figure can be barely distinguishable, we show the different fits separately in table 3 to illustrate how different fits can give rather similar results. The main differences in the outputs, as shown in table 4, come from the values of m_0 and, of course, of the enforced $\sigma_{\pi N}$. In addition, we also give in this table several other observables as in table 2. For the ratio R_c, the values given in table 3 agree with the experiment, eq. (3.2), within 5%, like in the case of A_4^+. It is worth stressing the perfect agreement with DEAR, concerning the energy shift and width for kaonic hydrogen, for all the fits of table 3, while, at the same time, all the scattering data shown in fig. 4, plus $\delta_{\pi\Lambda}(\Xi)$, m_0, $\sigma_{\pi N}$ and a_{0+}^+, are reproduced too.

The a_{K^-p} scattering lengths shown in the previous table are similar to those of the fit A_4^+ in table 2. Of course,

Table 4. Fits, given in table 3, that agree with the the DEAR data, eq. (3.4). The $\sigma_{\pi N}$ value enforced in the fits is given in the first row. The notation is like in table 2.

$\sigma_{\pi N}$	20^*	30^*	40^*
γ	2.36	2.36	2.37
R_c	0.629	0.628	0.628
R_n	0.168	0.171	0.173
ΔE (eV)	194	192	192
Γ (eV)	324	302	270
ΔE_D (eV)	204	204	207
Γ_D (eV)	361	338	305
a_{K^-p} (fm)	$-0.49+i\,0.44$	$-0.49+i\,0.41$	$-0.50+i\,0.37$
a_0 (fm)	$-1.07+i\,0.53$	$-1.04+i\,0.50$	$-1.02+i\,0.45$
a_1 (fm)	$0.44+i\,0.15$	$0.40+i\,0.15$	$0.33+i\,0.14$
$\delta_{\pi\Lambda}(\Xi)$ (°)	3.4	4.5	5.7
m_0 (GeV)	1.2	1.1	1.0
a^+_{0+} $(10^{-2}\cdot M_\pi^{-1})$	−2.0	−2.2	−2.2

they are much smaller in absolute value than those of fits B_4^+ and $\mathcal{O}(p)$. This is related to the fact that the new fits, as A_4^+, reproduce the DEAR data which, by the Deser formula, requires a much smaller scattering length than those of the fits B_4^+ and $\mathcal{O}(p)$. Let us recall that the A_4^+ fit of ref. [21] was the first chiral fit to be in agreement with the recent and accurate kaonic hydrogen data from ref. [1] and the scattering data of sect. 3. Nonetheless, since the fits in table 3 are also able to provide a good reproduction of the new precise data from refs. [23,24], they are preferred by us over the A_4^+ one.

It is remarkable as well the agreement with the measurement of $\delta_{\pi\Lambda}(\Xi)$ from refs. [73,74]. The values in table 4 are considerably larger than those obtained in ref. [83] from an $\mathcal{O}(p)$ analysis using UCHPT, where the range $-1.1^\circ \lesssim \delta_{\pi\Lambda} \lesssim 0^\circ$ was determined from an analysis of the scattering data of sect. 3. Hence we see that the effect of the higher orders in the kernel $\mathcal{T}$ are quite relevant for a precise determination of this quantity.

4.2 New B-type fits

Now, we report about other fits to the whole set of data that originate from the B_4^+ fit of ref. [21]. We also include here an $\mathcal{O}(p)$ fit to all the data of this section, except for the magnitudes in eq. (3.6), as they are defined in terms of the $\mathcal{O}(p^2)$ couplings. Following the same scheme of presentation as in the prior section, we enforce in the $\mathcal{O}(p^2)$ fits that $\sigma_{\pi N} = 20^*$, 30^* or 40^* MeV. The fitted parameters are given in table 5, while the results are shown in table 6 and in fig. 5 by the solid (40^*), dashed (30^*) and dash-dotted lines (20^*). The new $\mathcal{O}(p)$ fit is given in the last column of table 5 and its results are given in the last column of table 6 and in fig. 5 by the dotted lines.

We observe that all the fits in table 5 reproduce very well the scattering data, except for the $\mathcal{O}(p)$ fit which badly fails in the reproduction of $\sigma(K^-p\to\eta\Lambda)$, shown in the eighth panel. However, all these fits strongly disagree with the DEAR measurement, eq. (3.4), of the energy shift and width of the kaonic hydrogen, particularly for the former. It is also worth noticing that for the fits

Table 5. Fits, discussed in sect. 4.2, that do not agree with the DEAR data, eq. (3.4). The enforced $\sigma_{\pi N}$ value in the fit is shown in the first line.

Units	$\sigma_{\pi N}$ MeV	20^*	30^*	40^*	$\mathcal{O}(p)$
MeV	f	95.8	113.2	100.0	93.9
GeV^{-1}	b_0	−0.201	−0.159	−0.487	0^*
GeV^{-1}	b_D	−0.005	−0.297	0.127	0^*
GeV^{-1}	b_F	−0.133	−0.157	−0.188	0^*
GeV^{-1}	b_1	+0.122	+0.016	+0.135	0^*
GeV^{-1}	b_2	−0.080	−0.151	−0.037	0^*
GeV^{-1}	b_3	−0.533	−0.281	−0.494	0^*
GeV^{-1}	b_4	+0.028	−0.291	−0.173	0^*
	a_1	+4.037	+4.188	+2.930	−2.958
	a_2	−2.063	−3.129	−2.400	−1.479
	a_5	−1.131	−1.214	−1.225	−1.330
	a_7	−3.488	−3.000	−2.795	−1.805
	a_8	−0.347	+0.642	+2.906	−0.655
	a_9	−1.767	−2.109	−1.913	−1.918

in table 5 the corrections of eq. (3.5) over the Deser formula for Γ are large, around a 40%, see table 6, much larger than for the fits of table 3. In addition, the fits 20^*, 40^* and $\mathcal{O}(p)$ are also around 3 sigmas below the value of $\delta_{\pi\Lambda}(\Xi)$ measured in ref. [73]. For the fit 40^* the disagreement is at the level of 2 sigmas. All this seems to indicate that the fits of table 3 give a better overall reproduction of the data on $\bar{K}N$ scattering than those in table 5. Of course, the hypothetical confirmation of the DEAR data on the energy shift and width of kaonic hydrogen by the DEAR/SIDDHARTA Collaboration [2] will certainly refute the fits in table 5.

5 Spectroscopy

In this section we discuss in detail the pole content of our main fit, the last one in table 3. This fit will be referred in the following as I. We also present more briefly those poles corresponding to the 40^* and $\mathcal{O}(p)$ fits of table 5. The former will be called in the subsequent as II. Those

Table 6. Fits, given in table 5, that do not agree with the DEAR data, eq. (3.4). The notation is like in table 2.

$\sigma_{\pi N}$	20^*	30^*	40^*	$\mathcal{O}(p)$
γ	2.34	2.35	2.34	2.32
R_c	0.643	0.643	0.644	0.637
R_n	0.160	0.163	0.176	0.193
ΔE (eV)	436	409	450	348
Γ (eV)	614	681	591	611
ΔE_D (eV)	418	385	436	325
Γ_D (eV)	848	880	844	775
a_{K^-p} (fm)	$-1.01 + i\,1.03$	$-0.93 + i\,1.07$	$-1.06 + i\,1.02$	$-0.79 + i\,0.94$
a_0 (fm)	$-1.75 + i\,1.15$	$-1.65 + i\,1.30$	$-1.79 + i\,1.10$	$-1.50 + i\,1.00$
a_1 (fm)	$-0.13 + i\,0.39$	$-0.14 + i\,0.36$	$-0.12 + i\,0.46$	$0.32 + i\,0.46$
$\delta_{\pi\Lambda}(\Xi)$ ($^\circ$)	-1.4	1.7	-1.2	-1.4
m_0 (GeV)	0.8	0.6	0.7	...
a^+_{0+} ($10^{-2} \cdot M_\pi^{-1}$)	-0.5	-1.4	$+0.3$	...

other fits in tables 3 and 5 have a pole content very similar to that of the considered $\mathcal{O}(p^2)$ fits, I and II, respectively, and hence, we will not discuss them separately for the sake of brevity.

We only consider those Riemann sheets that are connected continuously to the physical sheet in some energy region of the physical axis. The physical Riemann sheet is such that the imaginary part of the modulus of the three-momentum associated with every channel is positive. The other Riemann sheets are defined depending on which three-momenta are evaluated in the other sheet of the square root, with an additional minus sign. The first non-physical Riemann sheet, 1RS, with $\mathrm{Im}\, p_1 \leq 0$, is reached when crossing the physical axis between the thresholds of $\pi\Lambda$ and $\pi\Sigma$, from 1.25 to 1.33 GeV, approximately[5]. The so-called second sheet, 2RS, with $\mathrm{Im}\, p_{1-4} \leq 0$, is reached when crossing the physical axis between the thresholds of $\pi\Sigma$ and $\bar{K}N$, around 1.34 and 1.43 GeV, respectively. The third sheet, 3RS, is connected continuously to the physical sheet between the thresholds of $\bar{K}N$ and $\eta\Lambda$, 1.44 and 1.66 GeV, approximately, and for this sheet $\mathrm{Im}\, p_{1-6} \leq 0$. The fourth sheet, 4RS, with $\mathrm{Im}\, p_{1-7} \leq 0$, can be reached when crossing the physical axis between the $\eta\Lambda$ and $\eta\Sigma$ thresholds, from around 1.66 to 1.74 GeV. The fifth sheet, 5RS, is connected to the physical one between the thresholds of $\eta\Sigma$ and $K\Xi$, around 1.74 and 1.81 GeV, respectively, and one has $\mathrm{Im}\, p_{1-8} \leq 0$. And finally, the sixth sheet, 6RS, with $\mathrm{Im}\, p_{1-10} \leq 0$, is reached by crossing the physical axis above the $K\Xi$ threshold, approximately at 1.81 GeV.

Once the pole position is known, one can then calculate the couplings by performing the limit

$$T_{ij} = \lim_{s \to s_R} -\frac{\gamma_i \gamma_j}{s - s_R}\ , \tag{5.1}$$

with s_R the pole position for the s Mandelstam variable. The γ_i is the coupling of the pole to the channel i_{th}.

[5] In the definition of the sheets we just talk about the $\bar{K}N$, $\pi\Sigma$ or $K\Xi$ thresholds, although in the physical case, because of isospin violation, each of these thresholds splits in several ones over a narrow region, less than 10 MeV wide at most. The indicated Riemann sheets apply below and above this narrow energy interval.

5.1 Fit I

– $I = 0$ *poles*: There are two $I = 0$ poles very close to the $\pi\Sigma$ threshold, one in the 1RS and the other in the 2RS sheet. They are located at $1301 - i\,13$ and $1309 - i\,13$ MeV, for the sheets 1RS and 2RS, respectively. The first pole has a small coupling[6] 1.12 to $\pi\Sigma$, while this coupling is large for the second pole, 3.68. This makes that the bump in the square of the $\pi\Sigma$ $I = 0$ amplitude is very asymmetric around the $\pi\Sigma$ threshold. On the left of this threshold one has the behaviour corresponding to 1RS, so that one observes basically a cusp effect with very little influence of the 1RS pole, while at the right of the threshold the behaviour is dominated by the falling at the right of the 2RS pole. This is illustrated in the first panel of fig. 6, from left to right and top to bottom, where the square modulus of the $I = 0$ $\pi\Sigma$ S-wave is shown. These two poles reflect the same resonance because they are connected continuously when passing softly via a continuous parameter from the 1RS to the 2RS, as we have checked. For the $\bar{K}N$ channel one has a peak at the 1RS pole position, although the opening of the $\pi\Sigma$ channel makes a strong cusp effect that distorts strongly the resonance shape giving rise to a sharp dip between the $\pi\Sigma$ thresholds along the right tail of the 2RS pole. On the 2RS we also have another pole at $1414 - i\,23$ MeV, with large couplings to $\pi\Sigma$ (4.24), $\bar{K}N$ (4.87) and $K\Xi$ (9.35). Note that all the ten coupled channels are degenerate in the $SU(3)$ limit and hence $SU(3)$, simply because of the Wigner-Eckart theorem, does permit large couplings of a resonance to much heavier channels than the resonance mass. This pole, 2RS 1414, gives rise to the "standard" $\Lambda(1405)$-resonance, clearly seen in the $\pi\Sigma$ event distributions of figs. 2, 4 and 5. Its width resulting from the pole position[7] is around 46 MeV. Their parameters, mass and width, are then in

[6] All couplings will be given in GeV.

[7] As it is well known, minus twice the imaginary part of the pole position is the width of the resonance. Nonetheless, this is only so when the resonance is narrow and its difference to the closest threshold is substantially larger than the width.

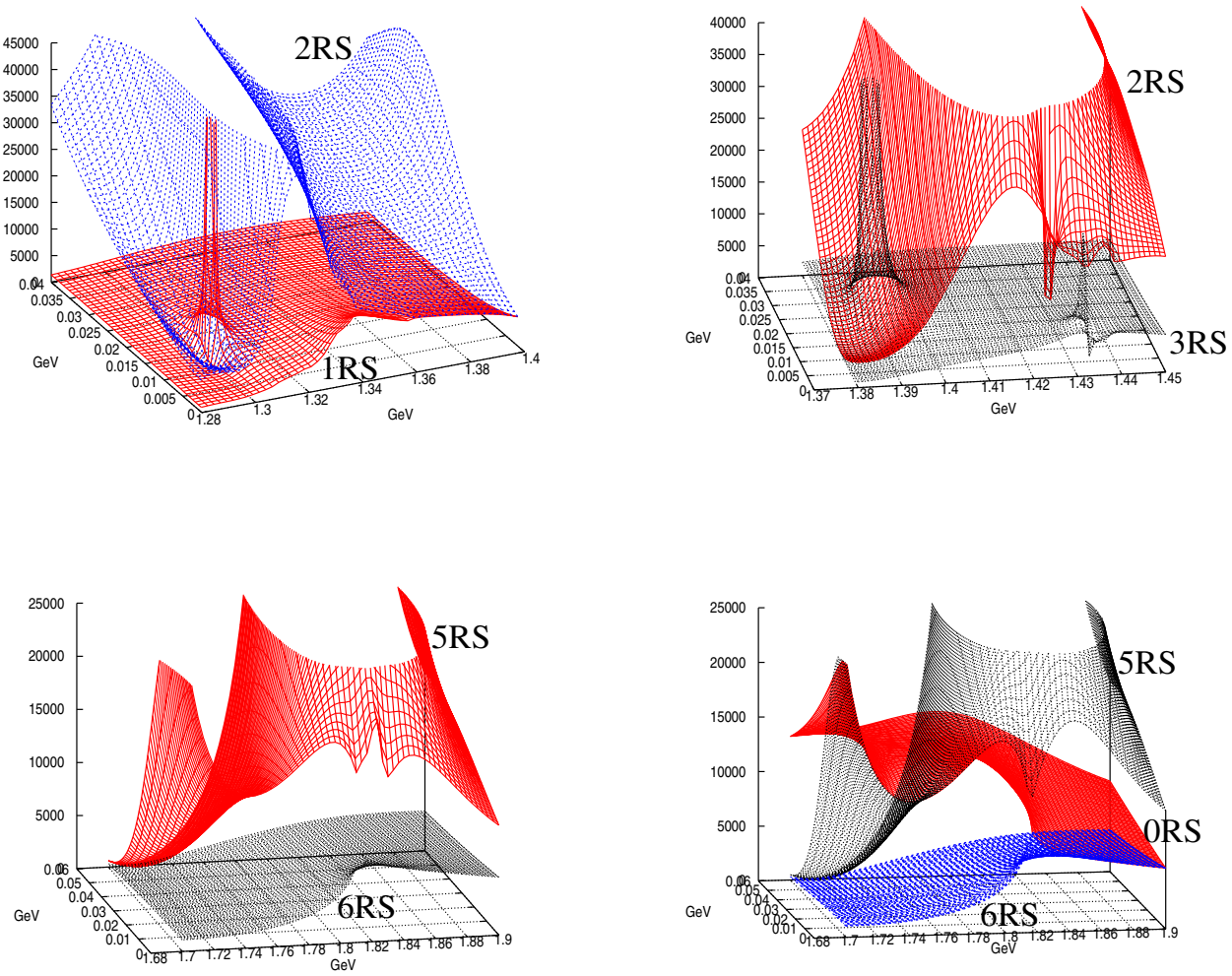

Fig. 6. Some poles with $I = 0$ for the fit I. From left to right and top to bottom, we have the square modulus of the $I = 0$ S-waves: $\pi\Sigma$, $\bar{K}N$, $K\Xi$ and of $K\Xi$ in the isospin limit.

Table 7. Fit I, $I = 0$ poles. The pole positions are given in MeV and the couplings in GeV. The symbol $|\gamma_i|_I$ means the coupling of the corresponding pole to the state with definite isospin I made up by the charged states of the i_{th} channel. The couplings to the $I = 1$, 2 channels are always close to zero.

Re(Pole) $\lvert\gamma_{\pi\Lambda}\rvert$	$-$Im(Pole) $\lvert\gamma_{\pi\Sigma}\rvert_0$	Sheet $\lvert\gamma_{\pi\Sigma}\rvert_1$	$\lvert\gamma_{\pi\Sigma}\rvert_2$	$\lvert\gamma_{\bar{K}N}\rvert_0$	$\lvert\gamma_{\bar{K}N}\rvert_1$	$\lvert\gamma_{\eta\Lambda}\rvert$	$\lvert\gamma_{\eta\Sigma}\rvert$	$\lvert\gamma_{K\Xi}\rvert_0$	$\lvert\gamma_{K\Xi}\rvert_1$
1301	13	1RS							
0.03	1.12	0.02	0.01	5.83	0.05	0.41	0.04	2.11	0.03
1309	13	2RS							
0.02	3.66	0.02	0.02	4.46	0.04	0.21	0.04	3.05	0.03
1414	23	2RS							
0.14	4.24	0.13	0.01	4.87	0.39	0.85	0.20	9.35	0.11
1388	17	3RS							
0.02	3.81	0.02	0.02	1.33	0.04	0.42	0.04	9.55	0.04
1676	10	3RS							
0.01	1.28	0.03	0.00	1.67	0.01	2.19	0.07	5.29	0.07
1673	18	4RS							
0.01	1.26	0.02	0.00	1.82	0.01	2.13	0.06	5.32	0.06
1825	49	5RS							
0.02	2.29	0.02	0.00	2.10	0.02	0.89	0.03	7.43	0.09

good agreement with those of the PDG [61]. The right most shape of this resonance, above the $\bar{K}N$ thresholds, does not correspond to any pole in the 3RS plane and just corresponds to a cusp effect due to the opening of the $\bar{K}N$ thresholds. This behaviour is shown in the second panel of fig. 6, where the square modulus of the $I = 0$ $\bar{K}N$ S-wave is plotted. In this panel one can also observe a narrow pole between the K^-p and $\bar{K}^0n$ thresholds corresponding to a narrow $I = 1$ pole to be discussed below. This pole appears in $I = 0$ because of isospin violation. In the 3RS we find another pole at $1388 - i\,17$ MeV that controls, modulo the cusp effect at the opening of the $\bar{K}N$ thresholds, the size of the $\pi\Sigma$ $I = 0$ amplitudes. This pole couples much more weakly to $\bar{K}N$, and this is why it does not affect its shape in the physical sheet, see the second panel. These two latter poles, 2RS 1414 and 3RS 1388, are connected continuously and, hence, reflect the same resonance, the $\Lambda(1405)$. As discussed above, before this resonance we also have another one, peaked around the $\pi\Sigma$ threshold. In ref. [18] the fact of having two nearby poles around the nominal mass of the $\Lambda(1405)$ was referred as the dynamics of the two $\Lambda(1405)$. In our solution we still find two resonances, but one of these "$\Lambda(1405)$" has moved to lower energies, and the two peaks can be distinguished now. We now consider the $\Lambda(1670)$-resonance [61], this is clearly visible in ref. [23] data on the reaction $K^-p \to \eta\Lambda$, as shown in the eighth panel of figs. 2, 4 and 5. The left part of this resonance, before the opening of the $\eta\Lambda$ threshold, is driven by the pole in the 3RS at $1676 - i\,10$ MeV, while the right part, above the $\eta\Lambda$ threshold, is driven by the pole in the 4RS at $1673 - i\,13.5$ MeV. Both poles have similar values for mass and width although they are not the same, which is specially relevant in this case since the width is rather small, around 20 MeV, and because of the nearby position of the $\eta\Lambda$ threshold. These poles have their largest couplings to the $\eta\Lambda$ and $K\Xi$ channels, around 2.1 and 5.3, respectively. We also warn that the actual shape of the $\Lambda(1670)$-resonance can depend strongly on the process. For example, for the square modulus of the $\bar{K}N$ or $\pi\Sigma$ elastic $I = 0$ scattering amplitudes, the peak is shifted to higher energies, towards 1.7 GeV, because of a strong distortion induced in these cases by the $\eta\Lambda$ channel. For this channel the $\Lambda(1670)$ appears as a clean strong enhancement. However, its shape is an asymmetric distorted Breit-Wigner resonance because on the left of the $\eta\Lambda$ threshold it has a width of around 20 MeV, from the 2RS 1676 pole, while on the right its width is larger, around 26 MeV, from the 4RS 1673 pole. The poles 3RS 1676 and 4RS 1673 are connected continuously, as one would expect. They reflect, as discussed, the $\Lambda(1670)$-resonance. In the 5RS there is another pole at $1825 - i\,49$ MeV. This pole drives through a few tens of MeV before the $K\Xi$ threshold an increase in the $I = 0$ amplitudes involving the $\pi\Sigma$, $\bar{K}N$ and $K\Xi$ $I = 0$ states to which it couples strongly, 2.3, 2.1 and 7.4, respectively. The coupling to $\eta\Lambda$ is much weaker, 0.9, and it does not give rise to any rapid movement for this case. This pole disappears in the 6RS, and for energies higher than the $K\Xi$ threshold one only has a remarkable cusp effect. This is accompanied by an important decrease in the values of the $I = 0$ amplitudes for those to which the previous pole strongly couples. See the third panel of fig. 6, where the square modulus of the elastic $I = 0$ $K\Xi$ S-wave is shown. In the PDG [61] there is an entry for the $\Lambda(1800)$-resonance with values for its mass and width in correspondence with the pole position just given. However, we must stress that its signal in any scattering amplitude is far from being that of a simple Breit-Wigner because it appears just on top of the $K\Xi$ threshold (the distance to that is much smaller than its width of around 100 MeV), and this pole appears in one sheet but not in the next one. *E.g.*, its value for the width as minus twice the imaginary part of the pole position is not appropriate for this case to the right of the $K\Xi$ threshold. In the last panel of fig. 6 we show the square modulus of the same amplitude as in the third panel but now, in addition, we also show the physical sheet, indicated by 0RS. It is remarkable how this sheet matches along the real axis, because of continuity, first to the 5RS and then, after the $K\Xi$ threshold, to the 6RS. To show this more clearly, we have plotted the amplitude in the isospin limit for this last panel, so that only one threshold is present. We give in table 7 the pole positions and couplings of the discussed $I = 0$ poles.

– $I = 1$ *poles*: In the 2RS we find two narrow $I = 1$ poles close to the $\bar{K}N$ thresholds. One located at $1425 - i\,6.5$ MeV and the other at $1468 - i\,13$ MeV. The former has a $\pi\Sigma$ coupling of 1.7 while the latter has a much stronger one of 6.0. They interfere destructively around 1.42 GeV and there is a dip there, as shown in the first panel of fig. 7, where the square modulus of the elastic $I = 1$ $\pi\Sigma$ S-wave is plotted. Indeed, this is the only observable signal in the square of the $I = 1$ $\pi\Sigma$ elastic amplitude for the second pole, because it disappears in the 3RS. Had the heavier pole not appeared we would then have obtained a symmetric and standard Breit-Wigner resonance shape for the pole at $1425 - i\,6.5$ MeV. Instead, we find a sharp dip to the right of the pole position. This remarkable destructive interference for the $\pi\Sigma$ and $\bar{K}N$ $I = 1$ amplitudes below the $\bar{K}N$ threshold is due to the large couplings of the pole in the 2RS at $1468 - i\,13$ MeV to $\pi\Sigma$ (6.0) and $\bar{K}N$ (8.7). This effect is not so strong in the $\pi\Lambda$ case because its coupling is smaller, 2.8. The 2RS pole $1425 - i\,6.5$ MeV evolves continuously in the 3RS to another pole at $1433 - i\,3.7$ MeV. This pole drives the behaviour of the $I = 1$ amplitudes at the right of the $\bar{K}N$ threshold. These two poles, being connected, correspond to the same resonance. We see then that the behaviour of the $I = 1$ amplitudes from around 1.4 up to 1.45 GeV is dominated by these three poles, giving rise to a pronounced peak structure in the amplitudes. Recently, a signal for a resonance at 1480 ± 15 MeV and width of 60 ± 15 MeV has been reported from

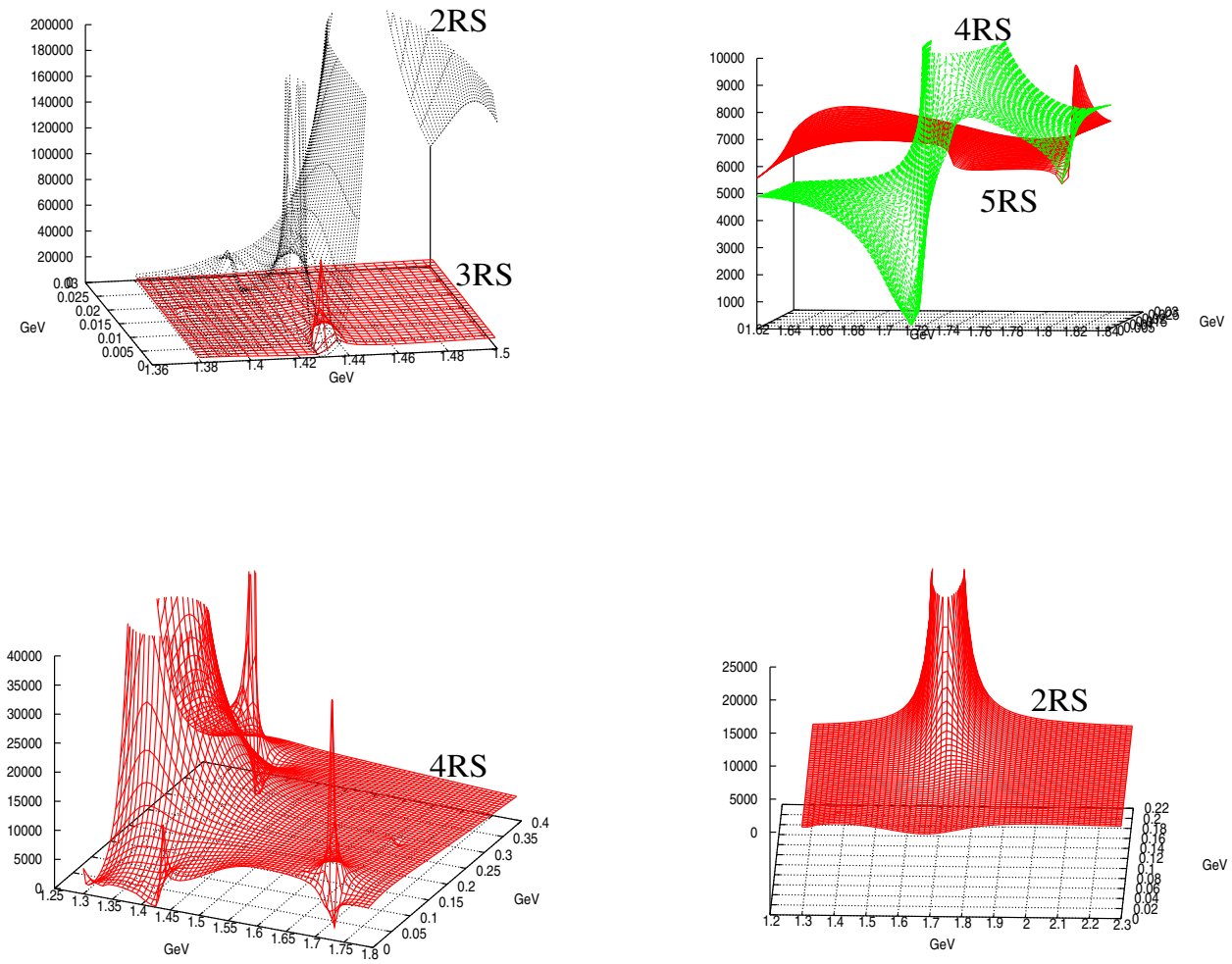

Fig. 7. Some poles with $I = 1$ for the fit I. From left to right and top to bottom, we have the square modulus of the $I = 1$ S-waves: $\pi\Sigma$, $\pi\Lambda$ and again of $\pi\Sigma$. The last panel corresponds to the square modulus of the $I = 2$ $\pi\Sigma$ S-wave.

Table 8. Fit I, $I = 1$ poles. The pole positions are given in MeV and the couplings in GeV. The couplings to the $I = 0$, 2 channels are always close to zero. The notation is like in table 7.

Re(Pole)	−Im(Pole)	Sheet							
$\lvert\gamma_{\pi\Lambda}\rvert$	$\lvert\gamma_{\pi\Sigma}\rvert_0$	$\lvert\gamma_{\pi\Sigma}\rvert_1$	$\lvert\gamma_{\pi\Sigma}\rvert_2$	$\lvert\gamma_{\bar{K}N}\rvert_0$	$\lvert\gamma_{\bar{K}N}\rvert_1$	$\lvert\gamma_{\eta\Lambda}\rvert$	$\lvert\gamma_{\eta\Sigma}\rvert$	$\lvert\gamma_{K\Xi}\rvert_0$	$\lvert\gamma_{K\Xi}\rvert_1$
1425	6.5	2RS							
1.35	0.24	1.66	0.01	0.35	3.92	0.05	4.23	0.49	2.98
1468	13	2RS							
2.80	0.16	5.96	0.02	0.23	8.74	0.04	10.66	0.19	2.48
1433	3.7	3RS							
0.65	0.08	0.80	0.00	0.12	1.58	0.02	5.82	0.20	2.14
1720	18	4RS							
1.82	0.02	1.21	0.00	0.02	0.95	0.02	6.78	0.05	5.31
1769	96	6RS							
2.65	0.00	0.61	0.00	0.00	2.48	0.00	3.32	0.01	4.22
1340	143	3-4RS							
1.33	0.14	5.50	0.02	0.02	1.58	0.00	3.28	0.03	1.20
1395	311	3-4RS							
2.08	0.01	1.49	0.01	0.00	1.24	0.00	7.63	0.01	3.97

the reaction $pp \to K^+ pY^{0*}$ in ref. [62]. Maybe, one can invoke interference effects to account for the displacement of our peak around 1.43 GeV to somewhat higher energies, as observed by COSY. Other relevant pole for the $I = 1$ amplitudes is the one located at $1720 - i\,18$ MeV on the 4RS. This pole is visible like a distorted bump in the $\pi\Lambda$ (1.82), $\pi\Sigma$ (1.21) and $\bar{K}N$ (0.95) S-waves, however is a clean resonance signal for the not yet open $\eta\Sigma$ (6.78) and $K\Xi$ (5.31) channels. In the 5RS this pole disappears and one only observes a $\eta\Sigma$ cusp effect in some channels whose value matches with the descending tail of the former pole in the 4RS. This enhancement corresponds to the $\Sigma(1750)$-resonance of the PDG, in good agreement with its values of mass and width. We show this behaviour in the second panel of fig. 7 by plotting the square modulus of the $\pi\Lambda$ S-wave. In the 6RS sheet we find a relevant pole at $1769 - i\,96$ MeV, with a width of around 200 MeV, which is responsible for the size and the slow descending value of the $I = 1$ amplitudes after the cusp around the $K\Xi$ thresholds. Hence, this pole cannot be observed directly as a bump in the physical axis. Regarding the $\Sigma(1620)$ [61], some of the $I = 1$ S-wave amplitudes show a broad bump after the $\bar{K}N$ threshold and before that of the $\eta\Sigma$. These bumps, like the one shown in the second panel of fig. 7 for the 5RS surface of the $\pi\Lambda$ elastic amplitude, is due to the interference of multiple poles. Two of them have been already discussed, namely, the 3RS 1433 and 4RS 1720 poles. In addition, there are other two broad poles at $1340 - i\,143$ and $1395 - i\,311$ MeV, shown in the last two lines of table 8, that appear simultaneously in the 3RS and 4RS in the same positions[8]. These poles, because of their long descending tails, control to a large extent the sizes of the $I = 1$ amplitudes in this region. All this produces this interesting interference phenomenon of soft bumps on the physical axis as shown also in the panel before the last one of fig. 7. In this panel the square modulus of the $\pi\Sigma$ elastic $I = 1$ S-wave is drawn. For this case, the wider pole is not very relevant, however, it is so for the $\eta\Sigma$ channel because its coupling to this channel is much larger than that of the lighter resonance at 1340 MeV. This is why we have kept it. The pole $1340 - i\,143$ MeV on the 3RS or 4RS sheets is connected continuously to the previous 2RS pole at $1468 - i\,13$ MeV, hence, for this solution, the $\Sigma(1620)$ and $\Sigma(1480)$ are clearly related. In table 8 we collect the different $I = 1$ poles for the fit I presented here.

– $I = 2$ *pole*: An exotic $I = 2$ pole appears at $1722 - i\,181$ MeV with a strong coupling to the $\pi\Sigma$ $I = 2$ channel (the only one possible with $I = 2$) of 6.18. This pole appears in the 2RS, 3RS, 4RS, 5RS and 6RS, since in all of them the momentum for the $\pi\Sigma$ has reversed sign and the only channel that matters is the $I = 2$ $\pi\Sigma$. This pole is actually the responsible for the $I = 2$ $\pi\Sigma$ size and gives rise to a soft and wide bump in the square modulus of the $I = 2$ amplitude, with a dip at 1.7 GeV due to a zero, see the last panel of fig. 6, where the square of the modulus of the $I = 2$ S-wave is shown. Because of this non-uniform shape and for its rather large magnitude, of the same order as that for the other isospin $\pi\Sigma$ channels, one can think of the possibility of detecting such exotic state.

[8] Notice that the $\eta\Lambda$ channel is $I = 0$ and this is why it does not appreciably modify the pole positions of these broad $I = 1$ poles.

5.2 Fits II and $\mathcal{O}(p)$

We consider here the pole content of the fits II and $\mathcal{O}(p)$, both fits are given in table 5. Tables 9 and 10 correspond to the $I = 0, 1$ poles of fit II, respectively, while the tables 11 and 12 are the same for the $\mathcal{O}(p)$ fit.

For the $I = 0$ poles of fit II we observe that the $\Lambda(1405)$ region is controlled by three poles, two in the 2RS and one in the 3RS. The first two control the shape before the $\bar{K}N$ threshold and the latter after this threshold is open. The 2RS 1347 and 3RS 1340 poles couple very strongly to $\pi\Sigma$ while the 2RS 1427 pole couples very strongly to $\bar{K}N$. Hence, the resonance looks broader for the $\pi\Sigma$ channel than for the $\bar{K}N$ one, since the resonance for the former mostly corresponds to the broader and lighter poles while for the latter it is mainly due to the narrower and heavier one. As a further consequence, for $\bar{K}N$ the resonance peak is shifted to the right. This kind of behaviour is already described in detail in ref. [18], where $\mathcal{O}(p)$ analyses were used. In addition, the two poles 2RS 1347 and 3RS 1340 are connected when passing continuously from the 2RS to the 3RS. The $\Lambda(1670)$-resonance is described by the two poles located in the same place both in the 4RS and 5RS, giving rise to a clean symmetric Breit-Wigner without asymmetries in the $\eta\Lambda$ threshold. Of course, these two poles are continuously connected. There is no signal for the $\Lambda(1800)$.

We now turn to the $I = 1$ poles for fit II. The region below the $\bar{K}N$ threshold is governed by the 2RS poles at $1399 - i\,41$ and $1424 - i\,3.6$ MeV. The latter appears as a dip in the slope of the former since the interference is destructive. Above the $\bar{K}N$ threshold one has again two poles, one broad and the other narrow, located in the 3RS at $1311 - i\,122$ and $1426 - i\,3$ MeV, respectively. In this case, the latter appears as a clear peak in the slope of the former. The 2RS 1399 and 3RS 1311 poles are connected continuously and then correspond to the same resonance. The same happens for the 2RS 1424 and 3RS 1426 poles, as one would expect. All these poles give rise to a broad enhancement of the $I = 1$ S-waves up to around 1.45 GeV. We do not observe any signal for the $\Sigma(1750)$. Regarding the $\Sigma(1620)$, a few amplitudes, like that of $\bar{K}N$, exhibits an enhancement around 1.6 GeV. Nonetheless, there is no a clear pole structure driving this behaviour. The most remarkable facts are the presence of a broad pole on the 3-4RS at $1311 - i\,122$ MeV, which controls, up to some extent, the size of the amplitudes in this region through its falling tail, and the opening of the $K\Xi$ channel, that always produce a pronounced cusp effect, sometimes like a bump others like a dip. Nonetheless, for fit I there were

Table 9. Fit II, $I = 0$ poles. The pole positions are given in MeV and the couplings in GeV. The notation is like in table 7.

Re(Pole)	−Im(Pole)	Sheet							
$\lvert\gamma_{\pi\Lambda}\rvert$	$\lvert\gamma_{\pi\Sigma}\rvert_0$	$\lvert\gamma_{\pi\Sigma}\rvert_1$	$\lvert\gamma_{\pi\Sigma}\rvert_2$	$\lvert\gamma_{\bar{K}N}\rvert_0$	$\lvert\gamma_{\bar{K}N}\rvert_1$	$\lvert\gamma_{\eta\Lambda}\rvert$	$\lvert\gamma_{\eta\Sigma}\rvert$	$\lvert\gamma_{K\Xi}\rvert_0$	$\lvert\gamma_{K\Xi}\rvert_1$
1347	36	2RS							
0.02	6.48	0.12	0.02	2.60	0.10	1.42	0.01	0.32	0.07
1427	18	2RS							
0.12	3.87	0.23	0.01	6.99	0.23	3.49	0.05	1.64	0.32
1340	41	3RS							
0.07	5.92	0.08	0.01	0.62	0.08	2.33	0.01	0.75	0.04
1667	8	4RS							
0.03	0.77	0.05	0.00	0.59	0.01	3.32	0.02	12.17	0.08
1667	8	5RS							
0.03	0.77	0.05	0.00	0.59	0.01	3.32	0.03	12.17	0.06

Table 10. Fit II, $I = 1$ poles. The pole positions are given in MeV and the couplings in GeV. The notation is like in table 7.

Re(Pole)	−Im(Pole)	Sheet							
$\lvert\gamma_{\pi\Lambda}\rvert$	$\lvert\gamma_{\pi\Sigma}\rvert_0$	$\lvert\gamma_{\pi\Sigma}\rvert_1$	$\lvert\gamma_{\pi\Sigma}\rvert_2$	$\lvert\gamma_{\bar{K}N}\rvert_0$	$\lvert\gamma_{\bar{K}N}\rvert_1$	$\lvert\gamma_{\eta\Lambda}\rvert$	$\lvert\gamma_{\eta\Sigma}\rvert$	$\lvert\gamma_{K\Xi}\rvert_0$	$\lvert\gamma_{K\Xi}\rvert_1$
1399	41	2RS							
1.49	0.09	5.58	0.01	0.13	4.92	0.08	0.73	0.03	4.99
1424	3.6	2RS							
0.54	0.14	1.58	0.00	0.20	1.17	0.10	0.61	0.04	3.76
1311	122	3-4RS							
2.63	0.05	4.61	0.01	0.02	3.44	0.02	0.60	0.03	3.60
1426	3	3RS							
0.56	0.04	1.18	0.00	0.07	0.77	0.04	0.61	0.02	3.74

Table 11. Fit $\mathcal{O}(p)$, $I = 0$ poles. The pole positions are given in MeV and the couplings in GeV. The notation is like in table 7.

Re(Pole)	−Im(Pole)	Sheet							
$\lvert\gamma_{\pi\Lambda}\rvert$	$\lvert\gamma_{\pi\Sigma}\rvert_0$	$\lvert\gamma_{\pi\Sigma}\rvert_1$	$\lvert\gamma_{\pi\Sigma}\rvert_2$	$\lvert\gamma_{\bar{K}N}\rvert_0$	$\lvert\gamma_{\bar{K}N}\rvert_1$	$\lvert\gamma_{\eta\Lambda}\rvert$	$\lvert\gamma_{\eta\Sigma}\rvert$	$\lvert\gamma_{K\Xi}\rvert_0$	$\lvert\gamma_{K\Xi}\rvert_1$
1375	60	2RS							
0.04	7.55	0.07	0.02	5.45	0.07	2.20	0.02	0.78	0.07
1429	22	2RS							
0.13	4.68	0.14	0.01	6.85	0.21	4.50	0.20	0.54	0.17
1710	19	4RS							
0.05	0.27	0.03	0.00	1.73	0.03	2.56	0.05	10.75	0.09
1710	19	5RS							
0.04	0.27	0.04	0.00	1.73	0.05	2.56	0.04	10.75	0.11

Table 12. Fit $\mathcal{O}(p)$, $I = 1$ poles. The pole positions are given in MeV and the couplings in GeV. The notation is like in table 7.

Re(Pole)	−Im(Pole)	Sheet							
$\lvert\gamma_{\pi\Lambda}\rvert$	$\lvert\gamma_{\pi\Sigma}\rvert_0$	$\lvert\gamma_{\pi\Sigma}\rvert_1$	$\lvert\gamma_{\pi\Sigma}\rvert_2$	$\lvert\gamma_{\bar{K}N}\rvert_0$	$\lvert\gamma_{\bar{K}N}\rvert_1$	$\lvert\gamma_{\eta\Lambda}\rvert$	$\lvert\gamma_{\eta\Sigma}\rvert$	$\lvert\gamma_{K\Xi}\rvert_0$	$\lvert\gamma_{K\Xi}\rvert_1$
1423	1.3	2RS							
0.52	0.12	0.72	0.00	0.18	1.28	0.11	1.49	0.02	2.30
1494	116	2RS							
3.83	0.15	10.06	0.03	0.14	9.25	0.06	2.82	0.02	4.55
1425	4.8	3RS							
0.93	0.05	1.22	0.00	0.11	1.63	0.07	2.71	0.01	3.43
1796	69	4RS							
3.97	0.01	2.33	0.01	0.02	1.96	0.03	3.20	0.15	9.09
1808	71	5RS							
3.71	0.01	1.94	0.00	0.01	2.36	0.02	1.15	0.11	8.16
1350	254	3-4RS							
2.38	0.06	5.19	0.01	0.02	3.36	0.01	5.33	0.01	4.11

more amplitudes manifesting bumps around 1.6 GeV than now for fit II.

We now consider the $\mathcal{O}(p)$ fit. The first $I = 0$ pole occurs at $1375 - i\,60$ MeV on the 2RS with a large coupling to $\pi\Sigma$. This pole interferes destructively with that at $1429 - i\,22$ MeV and this is why, at this point, the elastic $I = 0$ $\pi\Sigma$ S-wave has a dip. The latter pole couples very strongly with $\bar{K}N$ and it is seen as a clear maximum in the $\bar{K}N \to \pi\Sigma$ partial wave. There is no pole at around 1.4 GeV in the 3RS sheet and the right tail of this resonance, after the $\bar{K}N$ threshold, corresponds to a pronounced cusp effect that falls down from the latter threshold. Thus, for all the fits I, II and $\mathcal{O}(p)$ we observe the presence of a minimum in the $I = 0$ amplitudes before 1.42 GeV, a maximum for the modulus of the $I = 0$ $\pi\Sigma$ S-wave before such energy (for the fits I, II and $\mathcal{O}(p)$ the maximum is located around 1.34, 1.36 and 1.38 GeV, in order), and a maximum for the amplitudes involving the $\bar{K}N$ channel around its threshold. As discussed before, this is related to the so-called dynamics of the two $\Lambda(1405)$ [18]. The $\Lambda(1670)$ region is given by the poles 4RS and 5RS 1710, which have very similar properties and are continuously connected when passing from one sheet to the other. These poles describe this resonance above and below the $\eta\Sigma$ threshold, respectively. There is no signal for the $\Lambda(1800)$.

The narrow $I = 1$ pole 2RS 1423 only has an appreciable coupling to the $K\Xi$ channel, closed at such energies, and this is why it is so narrow. This pole appears as a dip in the increasing slope of the wide 2RS 1494 pole. In the 3RS one has another pole at $1424 - i\,4.8$ MeV, continuously connected to the 2RS 1423 one. As in fits I and II, all these poles give rise to a clear resonance structure up to around 1.5 GeV, close to the nominal mass of the $\Sigma(1480)$-resonance, and overlapping when taking into account widths [61]. In addition, the enhancement corresponding to the $\Sigma(1750)$ [61] appears again in this fit, as in fit I, and it corresponds to the relatively wide 4RS $1796 - i\,69$ and 5RS $1808 - i\,71$ MeV poles, in the relevant sheets for energies below and above the $\eta\Sigma$ threshold, respectively. These two poles are connected continuously. The $\Sigma(1620)$ bumps disappear for this fit. Although one has also here the mentioned resonances around the $\bar{K}N$ and $K\Xi$ thresholds, the amplitudes do not display bumps between them. One also has in the 3-4RS a wide pole at $1350 - i\,254$ MeV that interferes in the physical axis with the previous resonances but, in this case, this interference is negative, while in the fit I was positive. This pole is continuously connected to the 2RS 1494 pole.

Let us perform some $SU(3)$ considerations. Without moving to the $SU(3)$ limit, we calculate the interaction *kernels*, $\mathcal{T}$, appearing in eq. (2.5), for the $SU(3)$ irreducible representation **1**, **8s**, **8a**, **10**, $\overline{\mathbf{10}}$ and **27**. These are the ones that originate from the tensorial product $\mathbf{8} \otimes \mathbf{8}$ of the octets of baryons and mesons. If one performs such an exercise, one realizes that for the fit I the **1**, **8s**, **8a** and **27** have attractive kernels. These representations can accommodate four $I = 0$ and three $I = 1$ resonances, in agreement with the resonance content discussed above. For the fit II, one obtains attraction in the representations **1**, **8s**, **8a** and $\overline{\mathbf{10}}$. In this case, the previous $SU(3)$ representations can accommodate three $I = 0$ and 1 resonances, although only two $I = 1$ resonances finally appear. Similarly, for the $\mathcal{O}(p)$ fit one has attractive interaction in the representations **1**, **8s**, **8a** and $\overline{\mathbf{10}}$. As before these representations can accommodate three $I = 0$ and 1 resonances. This is in agreement with the fact that any of the latter two fits does not reproduce the $\Lambda(1800)$-resonance, while this is the case for the fit I.

We end this section with a general remark. The presence of poles in the physical Riemann sheet is forbidden because it violates hermiticity. However, although such poles could appear in approximate schemes (like ours), if they are wide enough their contributions on the real energy axis are soft and small and can be reabsorbed in the background. Let us make this statement more precise. Because of the Schwartz reflection principle, fulfilled by any partial wave, $T_L(W)^* = T_L(W^*)$, the poles always appear in complex conjugate positions on a given sheet with complex conjugate residua as well. Hence, if one performs a dispersion relation of a partial wave on the physical sheet, a pole does not contribute to the imaginary part, only to the real one, because it adds with its complex conjugate pole[9]. Thus, the presence of wide poles on the physical sheet can be considered as a minor problem of an approximate approach, since their relatively small contributions can always be removed and substituted by real polynomials of low degree in the dispersion relations for the physical amplitudes. This is not the case for true resonances, even wide ones, since they contribute to the imaginary part of the physical amplitudes, which is an input for the dispersion relation. For the fits I and II one observes the presence of two poles on the physical Riemann sheet, with $I = 0$ and 1, respectively, but with very large widths of around 300–400 MeV. These widths are much larger than those shown in tables 7, 8, 9 and 10 for the relevant poles that drive dominantly the behaviour of the physical amplitudes, as already discussed. Because of this and the argument just given, these wide resonances could be removed and replaced by low-degree polynomial backgrounds on the physical axis, keeping the rest of terms in the dispersion relations as given by our present solutions, which also fix the coefficients for these low-degree polynomials.

6 Conclusions

We have considered a wide set of experimental data that includes several K^-p cross-sections, namely, the elastic and charge exchange ones and productions of hyperons ($\pi^0\Lambda$, $\pi^0\Sigma^0$, $\pi^-\Sigma^+$ and $\pi^+\Sigma^-$), the $\pi\Sigma$ event distribution from ref. [60], the reaction $K^-p \to \pi^0\pi^0\Sigma^0$ from ref. [24], including a $\pi^0\Sigma^0$ event distribution and the total cross-section, the total cross-section of $K^-p \to \eta\Lambda$ [23],

[9] For our case we must take a subtractions since our partial waves goes like constant at infinity. It is enough to take the subtraction on the real axis so as the previous statement, about the real character of the pole contributions, is fulfilled.

three ratios γ, R_c and R_n of cross-sections at the threshold of K^-p [58,59], the difference of the P- and S-wave $\pi\Lambda$ phase shifts at the Ξ^- mass [73,74], $\delta_{\pi\Lambda}(\Xi)$, and the three quantities, m_p, a_{0+}^+, $\sigma_{\pi N}$, calculated at $\mathcal{O}(p^2)$ in baryon CHPT. Last, but not least, we have paid special attention to the energy shift and width of the α line ($2p \to 1s$) of kaonic hydrogen in connection to its recent and accurate measurement by the DEAR Collaboration [1]. We have reviewed the fits of ref. [21], including as well a new $\mathcal{O}(p)$ fit, and shown that they cannot reproduce the additional data considered in sect. 4, that is, those from $K^-p \to \pi^0\pi^0\Sigma^0$ [24] and from $K^-p \to \eta\Lambda$ [23]. These fits are given in table 1. We have then searched for new fits including from the beginning all the previous set of data points. Several fits arise, namely, the $\mathcal{O}(p^2)$ ones given in tables 3 and 5, that reproduce most of the data. The only exceptions are $\delta_{\pi\Lambda}(\Xi)$ and the DEAR data, eq. (3.4), that are not in agreement (within the present precision given by their last measurements from refs. [73] and [1], respectively) with the $\mathcal{O}(p^2)$ fits of table 5. The $\mathcal{O}(p)$ fit given in that table does not reproduce in addition the $K^-p \to \eta\Lambda$ total cross-section. Remarkably, the $\mathcal{O}(p^2)$ fits of table 3 are able to reproduce the whole set of data and, taking into account the value for $\sigma_{\pi N}$, around 50 MeV [68,34], we consider as our main fit, the so called fit I, the last one in this table with $\sigma_{\pi N} = 40^*$ MeV. Nonetheless, all of them give very similar results for the rest of quantities, as shown in fig. 4. Indeed, the values of the fitted free parameters are very similar, as shown in table 3. The values of the parameters of our main fit are quite similar to those of the fit A_4^+ of ref. [21] as well. This was the first fit to provide a set of chiral parameters leading to a simultaneous reproduction of the K^-p scattering data considered in ref. [21] and the DEAR value on the width and shift of kaonic hydrogen. In addition, we have analysed in detail the pole content of the fits I (main fit), II (the 40^* fit of table 5), and $\mathcal{O}(p)$ from table 5. We have discussed with special care the pole content of fit I and shown how it reproduces the two $\Lambda(1405)$ resonances, and the $\Lambda(1670)$, $\Lambda(1800)$, $\Sigma(1480)$, $\Sigma(1620)$ and $\Sigma(1750)$ resonances, as called in the PDG. We have shown that there is no one-to-one correspondence between poles and resonances and that the pole structure of a resonance can indeed be very involved, particularly, as it is always the case here, when there is a threshold in the nearby. One then must consider in detail the connection between Riemann sheets, in order to disentangle which poles are responsible for such effects, and collect as the same resonance those poles that are connected when passing continuously from one sheet to the other. Regarding the pole contents of fits II and $\mathcal{O}(p)$, the former does not contain any poles associated with the $\Lambda(1800)$ and the $\Sigma(1750)$ resonances, while the latter does not reproduce the $\Lambda(1800)$-resonance nor the $\Sigma(1620)$ bumps. Finally, fit I gives rise to an exotic broad $I = 2$ resonance that could be observed since its size is similar to that of the other $\pi\Sigma$ isospin S-waves, its shape is non-uniform and is the only resonance present in $I = 2$. Thus, also from the point of view of spectroscopy, fit I is the solution that fits better with the present resonance content in S-wave strangeness -1 as given in the PDG [61], giving rise to all the strangeness -1 S-wave resonances from the onset of the $\pi\Sigma$ channel up to energies above 1.8 GeV. We then conclude that fit I is our preferred solution in view of its unique agreement with the present experimental information on scattering, spectroscopy and kaonic hydrogen.

I would like to acknowledge fruitful discussions and common work with my collaborators J. Prades and M. Verbeni. I also thank E. Oset for useful discussions and communications. Financial support by MEC (Spain) grant No. FPA2004-03470, the European Commission (EC) RTN Program Network "EURIDICE" Contract No. HPRN-CT-2002-00311 and by the HadronPhysics I3 Project (EC) Contract No. RII3-CT-2004-506078 is acknowledged.

References

1. DEAR Collaboration (G. Beer *et al.*), Phys. Rev. Lett. **94**, 212302 (2005).
2. DEAR/SIDDHARTA Collaboration (D.L. Sirghi, F. Sirghi), *The physics of kaonic atoms at DAFNE*, `http://www.lnf.infn.it/esperimenti/dear/DEAR_RPR.pdf`; DEAR/SIDDHARTA Collaboration (C. Curceanu), *Precision measurements of kaonic atoms at DAFNE*, `www.tp2.ruhr-uni-bochum.de/vortraege/workshops/trento05/Petrascu.pdf`.
3. U.-G. Meißner, U. Raha, A. Rusetsky, Eur. Phys. J. C **35**, 349 (2004).
4. S. Deser *et al.*, Phys. Rev. **96**, 774 (1954); T.L. Trueman, Nucl. Phys. **26**, 57 (1961).
5. R.H. Dalitz, S.F. Tuan, Phys. Rev. Lett. **2**, 425 (1959); Ann. Phys. **8**, 100 (1959).
6. A.D. Martin, N.M. Queen, G. Violini, Nucl. Phys. B **10**, 481 (1969); P.M. Gensini, R. Hurtado, G. Violini, PiN Newslett. **13**, 291 (1997); B. Di Claudio, A.M. Rodriguez-Vargas, G. Violini, Z. Phys. C **3**, 75 (1979).
7. A.D. Martin, Nucl. Phys. B **179**, 33 (1979).
8. R. Buttgen, K. Holinde, J. Speth, Phys. Lett. B **163**, 305 (1985); R. Buettgen, K. Holinde, A. Mueller-Groeling, J. Speth, P. Wyborny, Nucl. Phys. A **506**, 586 (1990); A. Mueller-Groeling, K. Holinde, J. Speth, Nucl. Phys. A **513**, 557 (1990).
9. T. Hamaie, M. Arima, K. Masutani, Nucl. Phys. A **591**, 675 (1995).
10. P.J. Fink, G. He, R.H. Landau, J.W. Schnick, Phys. Rev. C **41**, 2720 (1990).
11. E.A. Veit, B.K. Jennings, R.C. Barrett, A.W. Thomas, Phys. Lett. B **137**, 415 (1984).
12. J.L. Goity, C.L. Schat, N.N. Scoccola, Phys. Rev. D **66**, 114014 (2002); Phys. Rev. Lett. **88**, 102002 (2002).
13. N. Kaiser, P.B. Siegel, W. Weise, Nucl. Phys. A **594**, 325 (1995).
14. J.A. Oller, E. Oset, Nucl. Phys. A **620**, 438 (1997); **652**, 407(E) (1999).
15. E. Oset, A. Ramos, Nucl. Phys. A **635**, 99 (1998).
16. J.A. Oller, E. Oset, A. Ramos, Prog. Part. Nucl. Phys. **45**, 157 (2000).

17. J.A. Oller, U.-G. Meißner, Phys. Lett. B **500**, 263 (2000).
18. D. Jido, J.A. Oller, E. Oset, A. Ramos, U.-G. Meißner, Nucl. Phys. A **725**, 181 (2003).
19. C. Garcia-Recio, M.F.M. Lutz, J. Nieves, Phys. Lett. B **582**, 49 (2004).
20. B. Borasoy, R. Nissler, W. Weise, Phys. Rev. Lett. **94**, 213401 (2005); Eur. Phys. J. A **25**, 79 (2005); Comment on *Surprises in threshold antikaon-nucleon physics*, arXiv:hep-ph/0512279.
21. J.A. Oller, J. Prades, M. Verbeni, Phys. Rev. Lett. **95**, 172502 (2005).
22. J.A. Oller, J. Prades, M. Verbeni, Reply to the comment on *Surprises in threshold antikaon-nucleon physics*, arXiv:hep-ph/0601109.
23. Crystal Ball Collaboration (A. Starostin *et al.*), Phys. Rev. C **64**, 055205 (2001).
24. Crystal Ball Collaboration (S. Prakhov *et al.*), Phys. Rev. C **70**, 034605 (2004).
25. V.K. Magas, E. Oset, A. Ramos, Phys. Rev. Lett. **95**, 052301 (2005).
26. D.B. Kaplan, A.E. Nelson, Phys. Lett. B **175**, 57 (1986).
27. G.Q. Li, C.H. Lee, G.E. Brown, Nucl. Phys. A **625**, 372 (1997).
28. J.A. Pons, S. Reddy, P.J. Ellis, M. Prakash, J.M. Lattimer, Phys. Rev. C **62**, 035803 (2000).
29. A. Sedrakian, *The physics of dense hadronic matter and compact stars*, arXiv:nucl-th/0601086.
30. KaoS Collaboration (W. Scheinast *et al.*), *First observation of in-medium effects on phase space distributions of antikaons measured in proton-nucleus collisions*, arXiv:nucl-ex/0512028; KaoS Collaboration (F. Laue *et al.*), Phys. Rev. Lett. **82**, 1640 (1999).
31. C. Fuchs, Prog. Part. Nucl. Phys. **56**, 1 (2006).
32. C. Garcia-Recio, E. Oset, A. Ramos, J. Nieves, Nucl. Phys. A **703**, 271 (2002); A. Baca, C. Garcia-Recio, J. Nieves, Nucl. Phys. A **673**, 335 (2000).
33. G0 Collaboration (D.S. Armstrong *et al.*), Phys. Rev. Lett. **95**, 092001 (2005); HAPPEX Collaboration (K.A. Aniol *et al.*), Phys. Rev. Lett. **96**, 022003 (2006); SAMPLE Collaboration (D.T. Spayde *et al.*), Phys. Lett. B **583**, 79 (2004); PVA4 Collaboration (F.E. Maas *et al.*), Phys. Rev. Lett. **94**, 152001 (2005).
34. M.M. Pavan *et al.*, PiN Newslett. **16**, 110 (2002).
35. S. Weinberg, Physica A **96**, 327 (1979).
36. J. Gasser, H. Leutwyler, Ann. Phys. **158**, 142 (1984); Nucl. Phys. B **250**, 465 (1985).
37. U.-G. Meißner, Rep. Prog. Phys. **56**, 903 (1993).
38. U.-G. Meißner, *Chiral QCD: baryon dynamics*, in *At the Frontier of Particle Physics*, edited by M. Shifman, vol. **1*** (World Scientific, 2002) pp. 417-505, arXiv:hep-ph/0007092.
39. V. Bernard, N. Kaiser, U.-G. Meißner, Int. J. Mod. Phys. E **4**, 193 (1995).
40. A. Pich, Rep. Prog. Phys. **58**, 563 (1995).
41. G. Ecker, Prog. Part. Nucl. Phys. **35**, 1 (1995).
42. J. Gasser, M.E. Sainio, A. Svarc, Nucl. Phys. B **307**, 779 (1988).
43. S. Weinberg, Nucl. Phys. B **363**, 3 (1991).
44. N. Kaiser, Phys. Rev. C **64**, 045204 (2001).
45. B. Borasoy, U.-G. Meißner, Ann. Phys. **254**, 192 (1997).
46. U.-G. Meißner, S. Steininger, Nucl. Phys. B **499**, 349 (1997).
47. J.A. Oller, E. Oset, J.R. Pelaez, Phys. Rev. Lett. **80**, 3452 (1998); Phys. Rev. D **59**, 074001; **60**, 099906(E) (1999).
48. J.A. Oller, E. Oset, Phys. Rev. D **60**, 074023 (1999).
49. U.-G. Meißner, J.A. Oller, Nucl. Phys. A **673**, 311 (2000).
50. P.G. Ratcliffe, Phys. Rev. D **59**, 014038 (1999).
51. J.A. Oller, J. Prades, M. Verbeni, in preparation.
52. W.E. Humphrey, R.R. Ross, Phys. Rev. **127**, 1305 (1962).
53. J.K. Kim, Phys. Rev. Lett. **14**, 29 (1965).
54. M. Sakitt *et al.*, Phys. Rev. **139**, B719 (1965).
55. J. Ciborowski *et al.*, J. Phys. G **8**, 13 (1982).
56. W. Kittel, G. Otter, I. Wacek, Phys. Lett. **21**, 349 (1966).
57. D. Evans *et al.*, J. Phys. G **9**, 885 (1983).
58. R.J. Nowak *et al.*, Nucl. Phys. B **139**, 61 (1978).
59. D. Tovee *et al.*, Nucl. Phys. B **33**, 493 (1971).
60. R.J. Hemmingway, Nucl. Phys. B **253**, 742 (1985).
61. Particle Data Group (S. Eidelman *et al.*), Phys. Lett. B **592**, 1 (2004).
62. I. Zychor *et al.*, Phys. Rev. Lett. **96**, 012002 (2006).
63. E. Oset, A. Ramos, C. Bennhold, Phys. Lett. B **527**, 99 (2002); **530**, 260(E) (2002).
64. M.F.M. Lutz, E.E. Kolomeitsev, Nucl. Phys. A **755**, 29 (2005).
65. M. Iwasaki *et al.*, Phys. Rev. Lett. **78**, 3067 (1997); T.M. Ito *et al.*, Phys. Rev. C **58**, 2366 (1998).
66. V. Bernard, N. Kaiser, U.-G. Meißner, Phys. Lett. B **309**, 421 (1993).
67. J. Gasser, Ann. Phys. **136**, 62 (1981).
68. J. Gasser, H. Leutwyler, M. Sainio, Phys. Lett. B **253**, 252 (1991).
69. M. Frink, U.-G. Meißner, I. Scheller, Eur. Phys. J. A **24**, 395 (2005); M. Frink, U.-G. Meißner, JHEP **0407**, 028 (2004).
70. H.C. Schröder *et al.*, Phys. Lett. B **469**, 25 (1999).
71. D.F. Baxter *et al.*, Nucl. Phys. B **67**, 125 (1973).
72. F. James, *Minuit reference manual* **D506** (1994).
73. HyperCP Collaboration (M. Huang *et al.*), Phys. Rev. Lett. **93**, 011802 (2004).
74. E756 Collaboration (A. Chakravorty *et al.*), Phys. Rev. Lett. **91**, 031601 (2003).
75. J. Tandean, A.W. Thomas, G. Valencia, Phys. Rev. D **64**, 014005 (2001).
76. R.F. Lebed, M.A. Luty, Phys. Lett. B **329**, 479 (1994).
77. J.F. Donoghue, B.R. Holstein, B. Borasoy, Phys. Rev. D **59**, 036002 (1999).
78. B.C. Lehnhart, J. Gegelia, S. Scherer, J. Phys. G **31**, 89 (2005).
79. A. Semke, M.F.M. Lutz, *Baryon self energies in the chiral loop expansion*, arXiv:nucl-th/0511061.
80. D.M. Manley *et al.*, Phys. Rev. Lett. **88**, 012002 (2002).
81. C. Garcia-Recio, J. Nieves, E. Ruiz Arriola, M.J. Vicente Vacas, Phys. Rev. D **67**, 076009 (2003).
82. T. Hyodo, A. Hosaka, E. Oset, A. Ramos, M.J. Vicente Vacas, Phys. Rev. C **70**, 034605 (2004).
83. U.-G. Meißner, J.A. Oller, Phys. Rev. D **64**, 014006 (2001).